Simulating thermal remediation in porous media

by

Sukhdeep K Shergill

B.Sc., Seattle University, 2019

Thesis Submitted in Partial Fulfillment of the
Requirements for the Degree of
Master of Science

in the
Department of Mathematics
Faculty of Science

SIMON FRASER UNIVERSITY
Fall 2022

Declaration of Committee

Name:	**Sukhdeep K Shergill**
Degree:	**Master of Science**
Thesis title:	**Simulating thermal remediation in porous media**
Committee:	**Chair:** Ralf Wittenberg Associate Professor, Mathematics
	JF Williams Supervisor Associate Professor, Mathematics
	John Stockie Committee Member Professor, Mathematics
	Nilima Nigam Examiner Professor, Mathematics

Abstract

Remediation techniques involving thermal treatment technologies, such as thermal conductive heating, are effective at removing non-aqueous phase liquids (NAPL) from soils. In this process, co-located cylindrical heaters and extractors are placed in the soil. As the soil heats up, the contaminants vaporize and are removed by the extractors. In this thesis, we present a numerical model for the remediation of contaminated soil. This numerical model couples a continuum model of the temperature in the soil with a macroscopic invasion percolation (Macro-IP) model to capture the dynamics of the gas migration. The heat transport is modelled using a finite difference scheme and Macro-IP uses constitutive relations to describe the fluid and gas phases. Finally, we compare the results of the Macro-IP model with a simpler Stefan problem in one dimension. The results show that the dynamics of the NAPL front are primarily determined by the time the location reaches a depth-dependent temperature, and only weakly on the amount of NAPL initially present. Moreover, it is unclear whether the additional model fidelity provided by including the Macro-IP step is necessary to make reasonable predictions of how long the heaters need to run.

Keywords: Porous media; thermal conductive heating; Macroscopic invasion percolation; Stefan problem

Acknowledgements

First and foremost, I would like to thank my supervisor Dr. JF Williams who made this work possible. His continuous guidance and support throughout this process is greatly appreciated.

I would like to extend my thanks to my thesis committee Dr. John Stockie, Dr. Nilima Nigam and Dr. Ralf Wittenburg for their insightful feedback and suggestions.

I am also thankful for my classmates and cohort for their words of encouragement and moral support.

Lastly, I would like to thank my friends and family for their love and support.

Table of Contents

List of Tables

List of Figures

Nomenclature

Constants

α	The ratio of the entry and terminal pressure	0.57
Δt	Time step	720s
Δx	Grid size	0.1m
Δz	Grid size	0.05m
Λ	Pore size distribution index	2.5
λ_{dry}	Thermal conductivity of dry soil	$0.15\mathrm{W} \cdot \mathrm{m}^{-1} \cdot \mathrm{K}^{-1}$
λ_{sat}	Thermal conductivity of saturated soil	$2.75\mathrm{W} \cdot \mathrm{m}^{-1} \cdot \mathrm{K}^{-1}$
ϕ	Porosity of soil is the void volume fraction in the porous media	0.3
ρ_n	Density of NAPL	$1.46\mathrm{g} \cdot \mathrm{cm}^{-3}$
ρ_s	Grain density	$2.7\mathrm{g} \cdot \mathrm{cm}^{-3}$
ρ_w	Density of water	$1\mathrm{g} \cdot \mathrm{cm}^{-3}$
σ	Gas-water interfacial tension	$0.0623\mathrm{N} \cdot \mathrm{m}^{-1}$
$C_{p,n}$	Specific heat capacity of NAPL	$0.8\mathrm{J} \cdot \mathrm{g}^{-1} \cdot \mathrm{K}^{-1}$
$C_{p,s}$	Specific heat capacity of soil	$0.958\mathrm{J} \cdot \mathrm{g}^{-1} \cdot \mathrm{K}^{-1}$
$C_{p,w}$	Specific heat capacity of water	$4.184\mathrm{J} \cdot \mathrm{g}^{-1} \cdot \mathrm{K}^{-1}$
k	Permeability of porous media	$\approx 10\mathrm{e}{-13}\mathrm{m}^2$
L_n	Latent heat of vaporization of NAPL	31.24kJ/mol
L_w	Latent heat of vaporization of water	41.47kJ/mol
L_x	Width of the domain	2.5 - 5m

L_z	Height of the domain	5 m
N_x	Number of grid points in x given by $L_x/\Delta x$	–
N_z	Number of grid points in z given by $L_z/\Delta z$	–
P_d	Displacement pressure	Pa
P_w	Water pressure	Pa
P_{cdim}	Dimensionless capillary pressure	0.18557
Q_H	Power of heater	$\mathrm{W \cdot m^{-2}}$
R	Ideal gas law	8.314462
S_r	Residual water saturation	0.13
S_{gcr}	Critical gas saturation	0.15
T^0	Initial temperature	10°C

Variables

$(\rho C_p)_e$	Effective heat capacity of soil-water-NAPL mixture	$\mathrm{J \cdot cm^{-3} \cdot K^{-1}}$
β	Thermal diffusivity given by $\lambda/(\rho C_p)_e$	$\mathrm{m^2 \cdot s^{-1}}$
λ	Thermal conductivity of soil	$\mathrm{W \cdot m^{-1} K^{-1}}$
P_c	Capillary pressure	Pa
P_g	Gas pressure	Pa
P_n^v	NAPL vapor pressure	Pa
P_w^v	Water vapor pressure	Pa
S_g	Saturation of gas	–
S_n	Saturation of NAPL	–
S_w	Saturation of water	–
T	Temperature of soil-water-NAPL mixture	°C

Chapter 1

Introduction

Soil contamination with petroleum and other heavy hydrocarbons is a major environmental problem and safety concern. Many contaminants can flow into the aquifer systems, contaminating the public water supply. Many sites are so contaminated that there is nowhere safe to send excavated soil. In addition, the depth at which some contaminants occur renders excavation prohibitively expensive, so other methods must be employed to remove the contaminants in situ. In urban settings, contaminated sites, like gas stations, are often left vacant for decades waiting for the site to become usable.

One rapid approach is in situ thermal remediation technology: the contaminated soil is heated up with an array of large heating devices, thus accelerating evaporation (and subsequent extraction) of the contaminants and cleaning the soil in a matter of months rather than years or decades. In areas with a high concentration of non-aqueous phase liquids (NAPL), in situ methods are typically more effective than conventional methods [9]. They have the advantage of shorter remediation times and high remediation rates. But heating contaminated soil to sufficiently high temperatures is an energy-intensive and costly endeavour, calling for a careful understanding of what is happening in the soil.

Some common in-situ technologies are steam-enhanced extraction (SEE), thermal conductive heating (TCH), electrical resistance heating (ERH), radio frequency heating (RFH) and free product thermal enhancement recovery. We focus on TCH treatments; these have the benefit of reaching higher temperatures, which makes it an ideal technology to use in large domains.

This thesis aims to examine a simulation technique typically used in the chemical engineering literature, to understand its convergence properties and implementation details, and to compare it with other simpler models to see if they can easily capture the most significant information.

The basic model is to use the heat equation to model the heat flux in the soil (dry or wet) and then use a model based on percolation theory to handle the movement of water and gases. The boiling of the contaminant and water is handled via energy balance in a manner similar to an enthalpy method for Stefan problems [11].

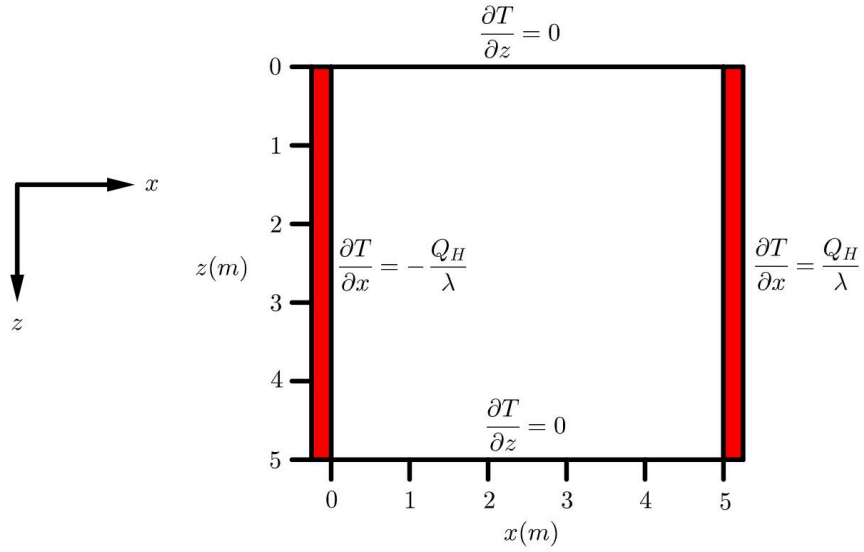

Figure 1.1: A 5m $\times$ 5m domain which is set up with z in the positive downward direction. The collocated heaters and extractors, shown in red, are located at the boundary of left and right wall of the domain. The heaters provide a constant heat flux at the left and right walls and we implement no heat flux at the top and bottom. In some simulations only the heater on the left will be turned on to better see the front propagate.

We will be implementing a model similar to [21] which is conducted over a rectangular domain of 20m $\times$ 5m. There are 5 heaters in the domain placed 5 meters apart. We will focus on a subsection of this region, a 5m $\times$ 5m domain with a heater on the left and right wall, as shown in Figure 1.1. The power of the heaters at the left and right wall are the same, so our simulations will be conducted over half the domain in x with only the left heater turned on. A simulation conducted with nonuniform NAPL saturation is shown in Figure 1.2.

There are other variations of the model. Our simulations model vertical cross sections but in [22] the simulations model horizontal cross sections. This requires solving the heat equation in radial coordinates. But the simulations were done on a small scale so the removal of vapors was instantaneous. Therefore this particular model was not coupled with Macro-IP. This model also considered multi-component NAPL but in our model we will only consider single-component NAPL. The model in [18] couples the continuum model for heating of the soil with Macro-IP but ERH is implemented instead of TCH. With ERH, the temperature of the domain is limited to about 120°C because it is restricted by the boiling point of water [22]. In Figure 1.2a, we can see that TCH can reach temperatures above that.

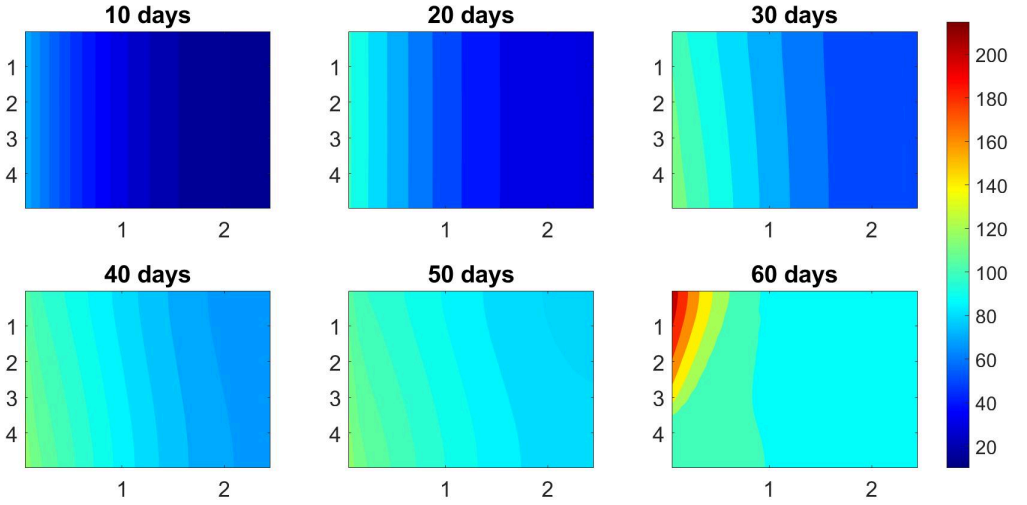

(a) Temperature profiles during the duration of the simulation. Initial temperature that was uniformly 10°C and after 60 days the max temperature was about 212°C. Thus range of the colorbar is from 10°C to 212°C.

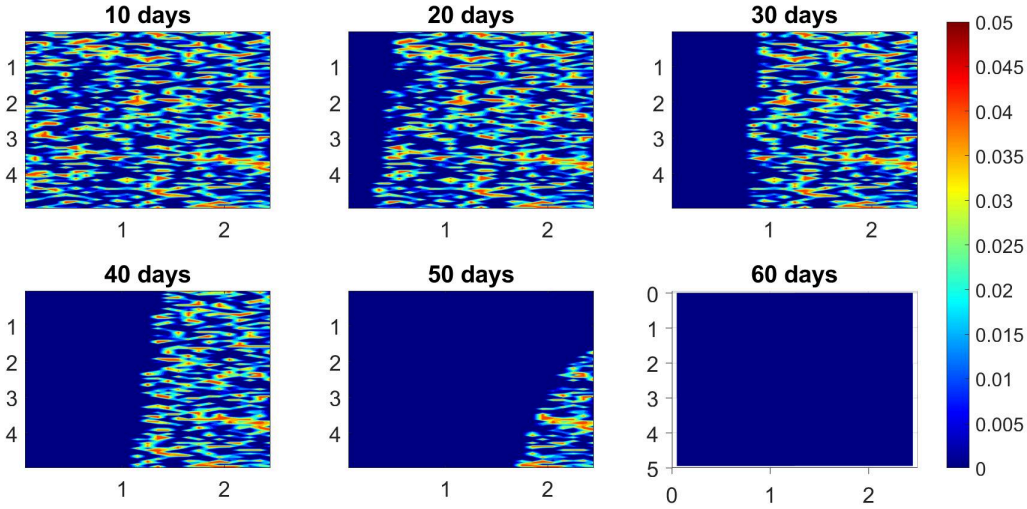

(b) NAPL profiles during the duration of the simulations. The initial saturation has values randomly chosen from the interval $[0, 0.05]$ with an average of 0.0145 in the entire domain. The colorbar is from 0 to 0.05. By 60 days all of the NAPL in the domain has been vaporized.

Figure 1.2: Temperature and NAPL saturation distributions for a simulation over a $5\text{m} \times 5\text{m}$ domain for 60 days. Only the left heater is turned on, so there was a constant heat flux and the other 3 walls had no heat flux.

1.1 Structure of the thesis

The goal of this thesis is to better understand the Macro-IP algorithm as it applies to this model and to compare it to some simplified PDE approaches for gleaning certain information.

We begin in Chapter 2 with some basic facts about porous media. These properties are required to understand some aspects of the formulation of the model. Chapter 3 describes the Thermal Conductive Heating model and how phase change is handled. We then describe the Macro-IP algorithm used to simulate fluid transport and how it differs from a continuous fluid model in Chapter 4. Chapter 5 describes the discretization of the heat equation and the implementation of Macro-IP. In Chapter 6 we construct some exact solutions to related simplified continuum models. Chapter 7 includes details of model validation: convergence to an exact solution, convergence to a high resolution numerical solution and comparison to published plots for parameter estimation. Chapter 8 presents some simulations and comparisons between the full model and a simplified Stefan problem.

Chapter 2

Porous Media Flow

The soil is modeled as a porous medium, which is a solid medium with void volume. The void volume allows fluid to flow through the medium and the study of this is known as porous media flow. In this Chapter we will describe some basic facts of flow in porous media as they will be needed to describe the phase changes in the thermal model and subsequent dynamics when using Macro-IP as that algorithm uses pressure differences to move and rearrange the mobile fluid states.

In one part of our model, we are essentially modelling the movement of two immiscible fluids, gas and water. Understanding how water and gas interact with each other is important in understanding the movement of gas vapors in our simulations. We will present details on the movement of a fluid in the presence of another by introducing details on capillary pressure and Darcy's law.

We'll introduce a few properties of porous media. In porous media, the porosity is a fraction that expresses the void volume of the porous medium

$$0 \leq \phi < 1.$$

We will assume a uniform porosity, but typically it is a nonuniform distribution. The void volume is occupied by one or more fluids. The saturation of fluid α, denoted as S_α, is the fraction of the void volume that is occupied by that fluid,

$$S_\alpha = \frac{V_\alpha}{V}, \qquad 0 \leq S_\alpha \leq 1$$

where V_α is the volume of the fluid and V is the void volume. In a medium that is fully saturated, the sum of the saturations must equal 1

$$\sum S_i = 1\,.$$

The permeability, denoted k, describes the porous medium's capacity for fluid movement. For the soils we are considering, typical values of k will range between $1\mathrm{e}-13$ to $5\mathrm{e}-09$ [2].

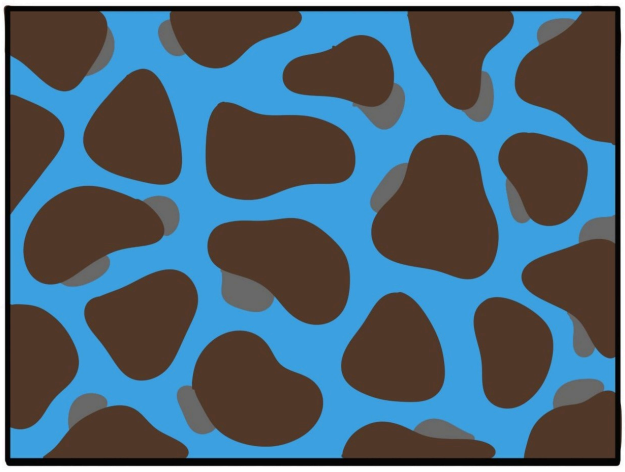

Figure 2.1: An example of the cell at the pore scale containing soil (brown), NAPL (gray), and water (blue). Gas phase is not shown but as water and NAPL are vaporized gas will fill the space.

Lower values of k in this range correspond to impermeable soil, which fluids have difficulty moving through. The permeability is usually expressed as a tensor, but we will assume it is constant.

2.1 Capillary Pressure

In a system with two immiscible fluids, we say that one of the fluids is the wetting fluid and the other is the non-wetting fluid. The interaction between the wetting and non-wetting fluid is described by capillary forces. In our simulations, water is the wetting fluid and gas is the non-wetting fluid, but the details on capillary pressure that will follow are introduced in the context of a general wetting and non-wetting fluid.

Consider a capillary tube in a domain with only water and air, as shown in Figure 2.2a. Capillary forces will cause the water to rise up in the tube and the interface between the two will create a contact angle with the surface of the capillary tube [4]. At the interface of two immiscible fluids in a capillary tube, the curvature of the interface can help us determine which of the two is the wetting fluid. The curvature is always concave towards the wetting fluid [7]. In Figure 2.2a the wetting fluid is water and non-wetting fluid is air, and in Figure 2.2b the wetting fluid is air and non-wetting fluid is mercury.

We can simplify a porous media to a capillary model, where the pore throats are capillary tubes [4]. The simplest models of porous media, such as used here, use a capillary model where void spaces are connected by capillary tubes.

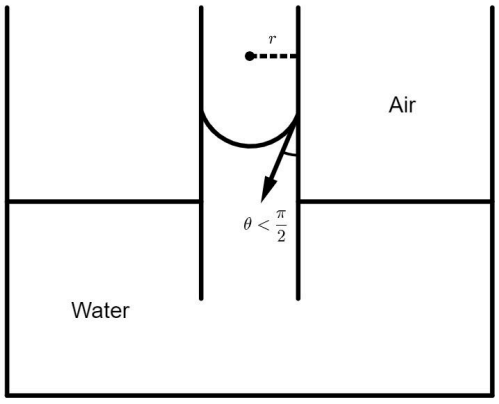

(a) Interface between air and water. The contact angle is less that $\pi/2$, so water is the wetting fluid.

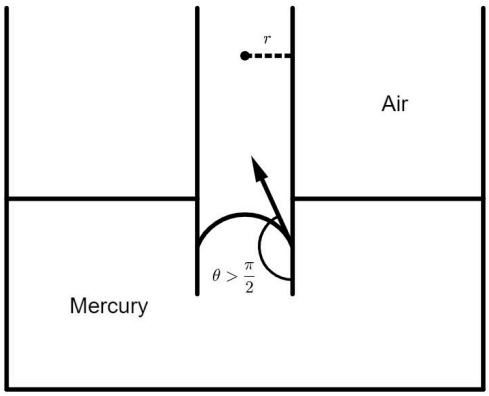

(b) Interface between air and mercury. The contact angle is greater than $\pi/2$, so air is the wetting fluid.

Figure 2.2: Interface of a wetting and non-wetting fluid in a capillary tube. In Figures 2.2a and 2.2b, the concavity of the interface can determine which fluid is the wetting and non-wetting fluids. In addition, the contact angle can also tell us which fluid is the wetting and non-wetting fluid.

The capillary force acting on the capillary tube is calculated using

$$F = 2\pi r\sigma\cos(\theta) \tag{2.1}$$

where σ is the interfacial tension, θ is the contact angle, and r is the radius of the capillary tube [23]. Then the capillary force can be used to compute the capillary pressure

$$P_c = \frac{2\sigma\cos(\theta)}{r}\,. \tag{2.2}$$

Consider an air-water system, there are upward and downward forces acting on the water column affecting the height of the water. The downward force is the capillary force while the upward force is gravity or buoyancy force. The capillary pressure can be computed using this balance of the upward and downward forces

$$P_c = H(G_w - G_a) \tag{2.3}$$

where H is the height of the water column, G_w is the water pressure gradient and G_a is the air pressure gradient.

The capillary pressure can also be expressed by the pressure difference between the wetting and non-wetting phase

$$P_c = P_N - P_W$$

where P_N and P_W are the pressure of the non-wetting and wetting phase respectively and $P_N > P_W$. The capillary pressure changes with the saturation of the fluids, so we can express the capillary pressure as function of saturation. There are multiple ways to define the relationship between capillary pressure and saturation, but we will use the Brooks-Corey relationship [8].

First, we can define the effective saturation, S_e, in terms of the capillary and bubbling pressure

$$S_e = \left(\frac{P_b}{P_c}\right)^{\Lambda} \tag{2.4}$$

where Λ is the pore size distribution index, P_b is the bubbling pressure and satisfies $P_c \geq P_b$. In theory, the pore size distribution index ranges from 0 to ∞ but in practice from about 1.8 to 7.3 [13]. Small Λ corresponds of a small range of pore sizes whereas a large Λ corresponds to a large range. The bubbling pressure is defined as the minimum capillary pressure at which a continuous non-wetting phase exists in a porous medium [7]. The effective saturation is

$$S_e = \frac{S_W - S_r}{1 - S_r} \tag{2.5}$$

where S_r is the irreducible wetting saturation which is the minimum saturation where the wetting phase is mobile. The wetting phase saturation must be in the range $S_r \leq S_W \leq 1$. As S_W approaches the irreducible wetting saturation, the effective permeability of the wetting phase approaches 0. So in each cell there will be some fluid that is immobile and trapped in the soil.

Combining (2.4) and (2.5) yields the Brooks-Corey $P_c - S_W$ relationship

$$P_c = \left(\frac{S_W - S_r}{1 - S_r}\right)^{-1/\Lambda} \cdot P_b \tag{2.6}$$

As S_W approaches 1, the capillary pressure approaches the bubbling pressure P_b.

The dynamics of water in soil is very complicated and can exhibit fingering, hysteresis, imbibition and more depending on whether the soil has recently been wet. We will stick to the assumptions in [20] and not consider other effects here.

2.2 Darcy's law

A basic equation that describes fluid flow through a porous media is the continuity equation,

$$\frac{\partial(\phi\rho S)}{dt} + \nabla \cdot (\rho v) = q \tag{2.7}$$

where v is the flow velocity and q is the source and sink term [1]. For low flow velocity, fluid flow can be modelled by Darcy's law, which is an empirical relationship between velocity

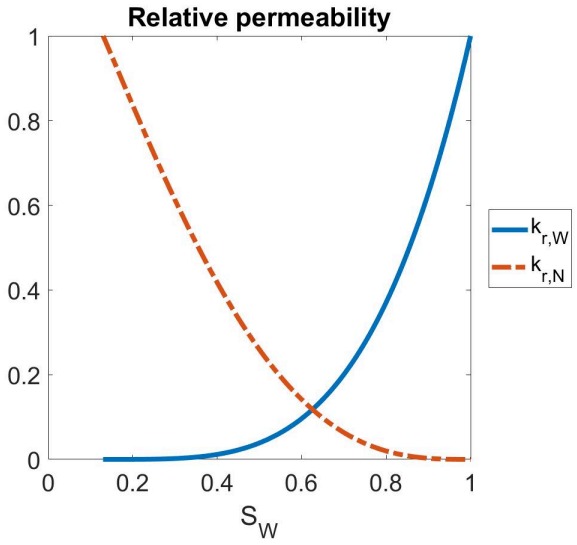

Figure 2.3: Plots of the Brooks-Corey relative permeabilities for water and NAPL (with $S_r = 0.13$)

and pressure. It is given by

$$q = -\frac{k}{\mu}\nabla(P - \rho g z) \tag{2.8}$$

where g is the acceleration due to gravity. We can express k in terms of the relative permeability of the fluid

$$k_{=}k_{ij}k_r. \tag{2.9}$$

where k is the permeability of the porous media and $0 \leq k_r \leq 1$ is the relative permeability. We assumed the permeability is just a constant so it does not have directional dependent effects. The relative permeability of a fluid is a nonlinear function of saturation that describes how the fluid moves in the presence of other fluids [1]. In a system where we have a wetting fluid and a non-wetting fluid the relative permeability for each phase is approximated by

$$k_{r,W} = S_e^{(2+3\Lambda)/2} \tag{2.10}$$

$$k_{r,N} = (1 - S_e)^2(1 - S_e^{(2-\Lambda)/\Lambda}) \tag{2.11}$$

Figure 2.3 shows the plots of the relative permeability as a function of the water saturation.

We will not solve Darcy's law-type equations directly. What is important is to recognize that changes in saturation are driven by differences in pressure. We will use the Macro-IP algorithm which implements rules based on mass and energy balance to discretely move the fluid. No PDEs are solved, instead cell pressures being above or below certain thresholds triggers certain actions.

Chapter 3

Thermal Conductive Heating Model

Our goal is to build a mathematical model for the remediation of soils using TCH. We will be conducting the simulations over a 5m $\times$ 5m vertical plane, with positive z in the downward direction. The collocated heaters and extractors are located on the left and right wall of the domain and extend across the entire vertical domain. The domain along with the collocated heaters and extractors are shown in Figure 1.1.

The model has two main components. The first models the heating of the soil with the heat transfer equation. There is a constant heat flux at the left and right wall due to the heaters, and there is no heat flux at the top and bottom of the domain [1]. We compute the heat flux at the left and right walls using Fourier's law of thermal conduction, which is given by

$$Q_H = \pm\lambda\nabla T \tag{3.1}$$

where Q_H is the power of the heaters, λ is the thermal conductivity and T is the temperature. The sign comes from the outward normal, at the left and right walls they are negative and positive, respectively. We will be using Q_H that gives us results consistent with [21]. Once the mixture reaches a certain temperature the liquid phases will turn into vapour. The gaseous states are mobile only once critical gas saturation is reached. This leads us to the second component of our model which is modelling the gas movement using a form of invasion percolation as described in Chapter 4.

[1] An extension of this model would incorporate a Robin condition at top surface as it is not perfectly insulated. In practice these devices run until the temperatures are over 600C and we rarely go much beyond that.

3.1 TCH model development

3.1.1 Heat transfer equation

The heating of the soil and liquid mixture is given by the conductive heat transfer equation

$$(\rho C_p)_e \frac{\partial T}{\partial t} = \nabla \cdot (\lambda \nabla T) - Q \tag{3.2}$$

where t is the time, Q is the heat source/sink term and $(\rho C_p)_e$ is the effective volumetric heat capacity. We implement no heat flux at the top and bottom walls of the domain

$$\left.\frac{\partial T}{\partial z}\right|_{z=0} = \left.\frac{\partial T}{\partial z}\right|_{z=5} = 0 \tag{3.3}$$

The left and right walls have a constant heat flux which are computed using (3.1),

$$\left.\frac{\partial T}{\partial x}\right|_{x=0} = -\frac{Q_H}{\lambda} \qquad \text{and} \qquad \left.\frac{\partial T}{\partial x}\right|_{x=5} = \frac{Q_H}{\lambda} \tag{3.4}$$

The effective volumetric heat capacity accounts for all of the constituent materials and is given by

$$(\rho C_p)_e = S_w \phi \rho_w C_{p,w} + S_n \phi \rho_n C_{p,n} + (1-\phi)\rho_s C_{p,s} \tag{3.5}$$

where ϕ is the porosity of the soil, S_α is the saturation, ρ_α is the density and $C_{p,\alpha}$ is the specific heat capacity for each component α. The thermal conductivity is a linear combination of the dry and saturated states

$$\lambda = K_e \left(\lambda_{sat} - \lambda_{dry}\right) + \lambda_{dry} \tag{3.6}$$

where $0 \leq K_e \leq 1$ is known as Kersten's number, and λ_{sat} and λ_{dry} are the thermal conductivities of saturation and dry soil. Kersten's number is dependent on the material parameters and gas saturation

$$K_e = \frac{\kappa(1-S_g)}{1+(\kappa-1)(1-S_g)} \tag{3.7}$$

where κ is a soil texture dependent parameter. The choice of κ will depend on the type of soil and whether it is frozen or unfrozen [10]. We will use $\kappa = 1.9$ as it best describes the relative permeability and saturation relationships of the unfrozen soil that we are using in our simulations [10]. This yields a weighted thermal conductivity [2] where

$$K_e \to 1 \text{ and } \lambda \to \lambda_{sat} \text{ as } S_g \to 0 \qquad \text{and} \qquad K_e \to 0 \text{ and } \lambda \to \lambda_{dry} \text{ as } S_g \to 1$$

[2] In some literature this may be referred to as a normalized thermal conductivity.

Substance	A_1 ($\log_{10}$(mmHg))	A_2 (°C $\cdot \log_{10}$(mmHg))	A_3 (°C)
Water	7.9492	1657.46	227.02
NAPL	6.87981	1157.83	202.58

Table 3.1: Antoine coefficients for water and NAPL [24]

Since the domain is initially fully saturated, Q is zero until gas production begins. Additionally, the heat capacity and thermal conductivity term depends on the saturations which do not change until co-boiling begins. Thus, up until co-boiling we are solving the two dimensional heat equation with a variable coefficient that depends on space.

3.1.2 Co-boiling

The water-NAPL-soil mixture is heated until it reaches a critical value, which is the pressure-dependent temperature at which water and NAPL vapor can start vaporizing. This process is called co-boiling and, surprisingly, allows for water and NAPL vapor to be produced at a temperature lower than the boiling point of either fluid. The soil mixture starts co-boiling[3] when the following is satisfied

$$P_w^v + P_n^v = P_w + P_d \tag{3.8}$$

where P_α^v is the vapor pressure, P_w is the water pressure, and P_d is the displacement pressure [21].

The vapor pressures can be estimated using the empirically derived Antoine equation, which is a monotonically increasing function of T given by

$$P_\alpha^v = 10^{\left(A_1 - \frac{A_2}{T + A_3}\right)} \tag{3.9}$$

The A_i's are called Antoine coefficients and are chosen to best fit experimental data. This equation gives P_α^v in mmHg, so we would need to convert this to Pa by multiplying (3.9) by $133.322\text{Pa} \cdot \text{mmHg}^{-1}$. The Antoine coefficients for water and NAPL are given in Table (3.1). In cells where no fluid is present the vapor pressure is set to zero.

Figure 3.2 shows a plot of the boiling temperature as a function of z where we have taken uniform values for the saturations, porosity, and permeability as

$$S_n \equiv 0.01, \quad S_w \equiv 0.99, \quad \phi \equiv 0.3, \quad \text{and} \quad k \equiv 1.03151\text{e} - 12\,.$$

The water and NAPL mixture has a lower boiling temperature than water or NAPL, so water and NAPL mixture vapor can be produced at a temperature lower than the boiling

[3]Co-boiling is a common term in this field for when two liquids boil at the same time.

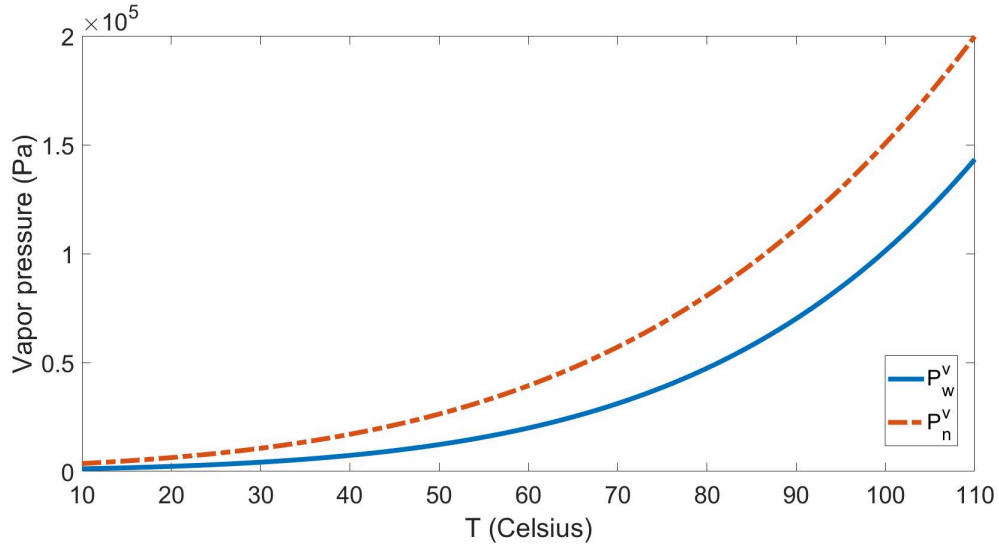

Figure 3.1: Plots of the water and NAPL vapor pressures in the range $10 - 110°C$

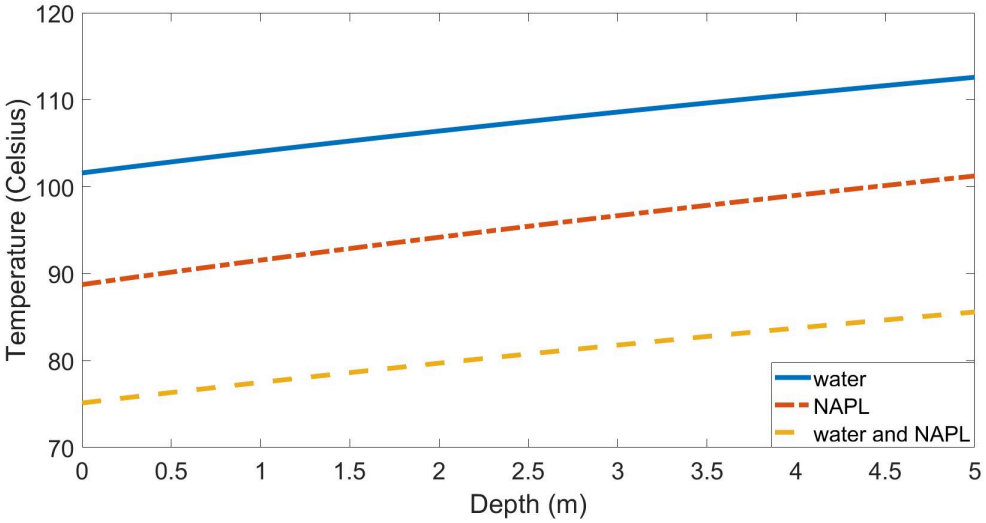

Figure 3.2: Plot of the temperature at which boiling and co-boiling begins as a function of depth.

point of water or NAPL. Additionally, for all 3 curves the boiling temperature increases with depth as the pressures increase with depth.

When a cell reaches its co-boiling temperature, the energy that was used for heating the water-NAPL-soil mixture is now used to produce water and NAPL vapor. In that cell the temperature will plateau and we compute Q by substituting $\partial T/\partial t = 0$ into (3.2). In co-boiling cells, the heat sink term is

$$Q = \nabla \cdot (\lambda \nabla T) \tag{3.10}$$

We can calculate the moles of gas produced using the energy balance and Dalton's law. The energy balance is given by

$$L_w n_{g,w} + L_n n_{g,n} = \int_{t^l}^{t^{l+1}} \int_V Q \, dV dt \tag{3.11}$$

$$Q = \frac{L_w n_{g,w} + L_n n_{g,n}}{V \Delta t} \tag{3.12}$$

where L_α is the latent heat for evaporation, $n_{g,\alpha}$ is the moles of gas produced, and V is the volume of the cell. Dalton's law is

$$\frac{n_{g,w}}{n_{g,n}} = \frac{P_w^v}{P_n^V} \tag{3.13}$$

We now use chemical and thermodynamical properties to close the system. The ideal gas law relates the moles of gas to volume of gas

$$V_g = \frac{(n_{g,w} + n_{g,n})RT}{P_g} \tag{3.14}$$

where R is the gas constant and P_g is the gas pressure. We assume liquid NAPL is immobile so we take water be the wetting phase fluid and the vapor be the non-wetting phase fluid. Using (2.1) we can express the gas pressure as the sum of the capillary and water pressure

$$P_g = P_c + P_w. \tag{3.15}$$

The water pressure is given by

$$P_w = \rho_w g h + P_w(h_0) \tag{3.16}$$

where g is the acceleration due to gravity, h is the height of water, and $P_w(h_0)$ is the water pressure at the top of the domain [20]. For the capillary pressure we will use the Brooks-Corey $P_c - S_w$ relationship given by (2.6), but we will need to make an adjustment to account for the immobile NAPL. We follow reference [21] and add the NAPL saturation to the irreducible wetting phase saturation to get the following

$$P_c = \left(\frac{S_w - S_r}{1 - S_r'} \right)^{-1/\Lambda} \cdot P_d \tag{3.17}$$

where $S_r' = S_r + S_n$ is the modified irreducible wetting phase saturation and P_d is the displacement pressure. The displacement pressure follows from Leverett's $J-$function [12] and is given by

$$P_d = P_{cdim} \sigma \sqrt{\frac{\phi}{k}} \tag{3.18}$$

Here P_{cdim} is dimensionless capillary pressure, σ is the gas-water interfacial tension, and k is the intrinsic permeability.

This gives us a method to heat the soil and boil off any liquid components in a cell. This approach is equivalent to an Enthalpy method for solving Stefan-like phase change problems, [11, 15] but with two key differences. First, rather than increasing the enthalpy until enough energy has been added to boil the contents of a cell we convert liquid into gas until there is none left or we are no longer at the pressure-dependent boiling temperature. Secondly, we can boil multiple cells at once with no additional modifications. The movement of gas is modelled using macroscopic invasion percolation (Macro-IP). In Macro-IP, adjacent gas occupied cells that exceed the critical gas saturation may merge or migrate.

Chapter 4

Macroscopic Invasion Percolation

The second component to our model facilitates the movement of gas. We are essentially modelling the displacement of a wetting fluid (water) by a non-wetting fluid (gas) *as it is being generated*. To avoid handling the creation and destruction of gas in a continuum model, or tracking interfaces, one can simply rearrange the fluid mechanistically. There are a few continuum models that can model discontinuous gas flow such as [16], but the Macroscopic Invasion Percolation (Macro-IP) algorithm has the advantage of being able to capture the *essential* physics at a lower computational cost [19]. Using MIP, the movement of gas is governed by drainage and imbibition thresholds, which are dependent on the pressures and saturations of the fluid. Once above or below certain thresholds multiple cells are joined together and their properties appropriately averaged.

Macro-IP is based on invasion percolation theory, which is a form of percolation theory that uses network models to model the flow of two immiscible fluids. We will first review percolation theory and its application to porous media flow. Then we will describe the relationships that govern the movement of gas in Macro-IP and its' application to this setting.

4.1 Invasion Percolation Theory

Invasion percolation (IP) theory is based on percolation theory, which is a a branch of statistics and probability that deals with fluid transport in porous media with random properties. Consider a square lattice shown in Figure 4.1, the intersection of the lines are called sites and the segments connecting sites are called bonds. We let sites either be open or closed and the openness of a site is independent of its neighbors. A group of connected sites are called clusters. The properties of the system are determined by the connectivity of sites and bonds [6]. Since the properties of the porous media are random, the openness of sites and bonds are assigned randomly.

IP theory uses a pore network model to describe the flow of two immiscible fluids. We can represent the porous media as a network where the pore bodies and capillary tubes represent

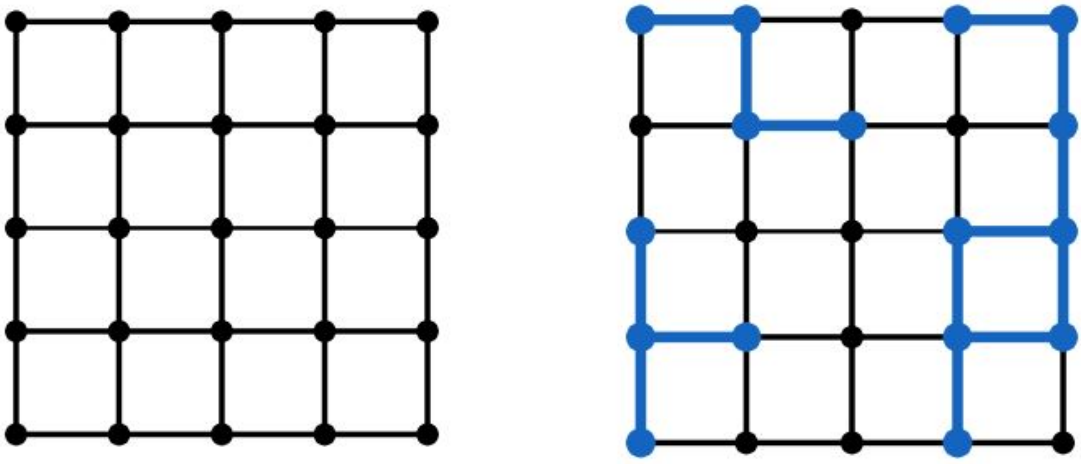

Figure 4.1: Two dimensional square lattices where the points are sites and the lines connecting them are bonds. In the image on the right blue sites and bonds represent open sites and bonds.

sites and bonds respectively, as shown in Figure 4.2. Like percolation theory, sites and bonds are either open or closed, and the movement of fluid is governed by the connectivity of the network. In IP theory, one of the two fluids is defined to be the 'invading' fluid and the other is the 'defending' fluid. So IP theory, models the infiltration of the invading fluid in the presence of the defending fluid. Network models can give us an understanding of fluids at the pore scale, but percolation theory allows us to do the same at a larger scale in an averaged sense.

4.1.1 IP vs Macro-IP

Macro-IP models the movement of gas in the presences of water, so we let gas and water be the invading and defending fluids, respectively. Invasion percolation models focus on fluid flow at individual capillary tubes (sub $mm-$scale) and bodies but with Macro-IP we will focus on average behaviour in sub regions of the porous medium ($mm - cm$ scale). Darcy's law determines continuous fluxes based on pressure gradients. Macro-IP models use the same idea 'pressure differences move material' but now replaces gradients with discrete thresholds.

4.2 Pressure and Thresholds

The movement of gas clusters is governed by drainage and imbibition thresholds, which are dependent on entry and terminal pressures across the bonds. The entry pressure (P_e) is the

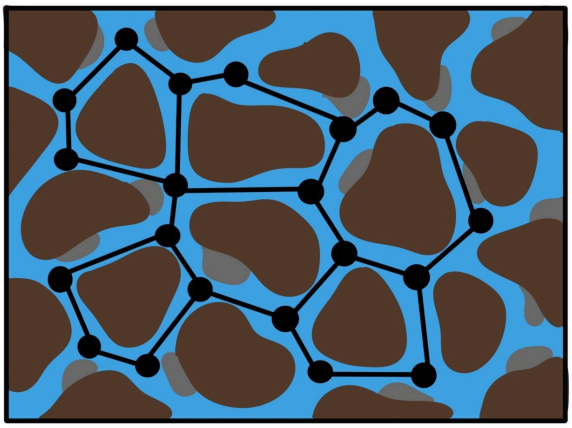

Figure 4.2: A porous medium where the pore bodies and throats are depicted as sites and bonds respectively.

pressure required for a clusters to invade a cell, this is given by

$$P_e = P_c S_w \tag{4.1}$$

The terminal pressure (P_t) is the pressure required for a cell to imbibe and it is given by

$$P_t = \alpha P_e \tag{4.2}$$

where α is a material dependent parameter based on capillary pressure measurements and is considered uniform throughout the domain [17]. Across various soils and fluids occupying the medium, α ranged from 0.44 to 0.71 [14]. We will be implementing Macro-IP with $\alpha = 0.57$ [20].

Then using the entry and terminal pressures we can define the thresholds for drainage and imbibition. The threshold for drainage is

$$T^e = P^e + P_w \tag{4.3}$$

and the threshold for imbibition is

$$T^t = P_t + P_w \tag{4.4}$$

We check these thresholds in each cell and then rearrange material as appropriate.

4.3 Processes

There are several different ways that cells can join or leave clusters and we need to implement each carefully. First, we define a critical gas saturation, S_{gcr}, which we assume is uniform

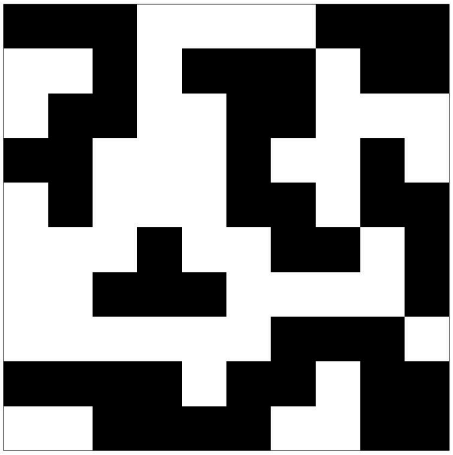

Figure 4.3: A visual of clusters in a domain with 10×10 cells. The black cells represent gas occupied cells where $S_g \geq S_{gcr}$. Only cells that share a face form a cluster so in this domain there are 6 clusters. The cluster at the bottom spans across the horizontal domain so NAPL vapor can travel from left to right. But since there isn't a cluster spanning across the vertical domain it can't travel from top to bottom.

throughout the domain. The critical gas saturation is the minimum gas saturation for gas transport to occur. Adjacent gas occupied cells where $S_g \geq S_{gcr}$ can be thought of as open sites. The connection between these open sites can be thought of as open bonds. So groups of connected cells are clusters. Only cells that share faces form a cluster. For example, in Figure 4.3 the domain has 6 clusters.

Then in each cell we define an entry and terminal pressure which dictates the expansion and mobilization of clusters. The process of expansion and mobilization/fragmentation repeats until we can no longer do so and the distribution has stabilized.

4.3.1 Expansion

Expansion occurs when the cluster's gas pressure is greater than the threshold for drainage in any adjacent cells. When an expansion event occurs there is an increase in volume and decrease in gas pressure. An example is shown in Figure 4.4a.

4.3.2 Mobilization and fragmentation

One difference between expansion and mobilization is that when a cluster expands the volume of gas increases whereas during mobilization the volume of the cluster remains the same. For a cluster to mobilize, first the condition for expansion must be satisfied. Next, the imbibition threshold of a cell in a cluster must be greater than the drainage threshold in any cell adjacent to the cluster. Figure 4.4b shows one example of mobilization. After a

mobilization event, the gas pressure in the invading block must be adjusted. Using the ideal gas law the gas pressure in cell 4 (shown in Figure 4.4b) is adjusted to

$$P_{g,4} = \frac{P_{g,1} S_{g,1} T_4}{T_1 S_{gcr}}$$

During a mobilization event fragmentation can also occur, as shown in Figure 4.4c. Fragmentation occurs when the imbibed cell is located within a cluster and it breaks a connection to other cells in the cluster. For both mobilization and fragmentation, the gas saturation in the imbibed cell is decreased to the residual gas saturation. This represents gas trapped in an imbibed cell after mobilization or fragmentation.

4.4 Redistribution

At the start of Macro-IP and after each expansion or mobilization/fragmentation event we need to redistribute the mass across the cluster. We want the gas pressure across the cluster to be constant. This requires us to solve a system of equations where mass is conserved and the local relationship between capillary pressure and water saturation is satisfied for all the cells across the cluster [21].

4.4.1 Collapse check

Once the cluster can't expand or mobilize each cell will undergo a collapse check. A cell collapses if the confining pressure, which is the sum of the capillary and water pressure, is greater than the total gas pressure. This will either occur because of high capillary pressures or cold temperatures. If a cell collapses, the saturation is zero and any gaseous mass is added to the aqueous phase [18].

4.4.2 Implementation

To define the clusters, we used Matlab's Image Processing toolbox. First, we created a logical array that satisfied $S_g \geq S_{gcr}$, where cells that satisfy this were labelled 1 and the rest 0. This array was used to generate a binary image where the cells that are labelled 1 are colored black and the rest were white, as shown in Figure 4.3. Then we use the bwlabel command that returns the number of clusters and a matrix with each cluster labelled. After the clusters are defined, the mass is redistributed so that the gas pressure is constant across the cluster. During redistribution, we assume that the NAPL vapor has a uniform concentration across each cluster and that liquid phases are immobile. Then we check if the cluster can expand or mobilize. We check for expansion first then mobilization/fragmentation, but the processes are assumed to occur instantaneously.

After each process, the gas saturation in the invaded block is increased to S_{gcr} and we redistribute the mass again. This process is repeated until clusters can no longer expand

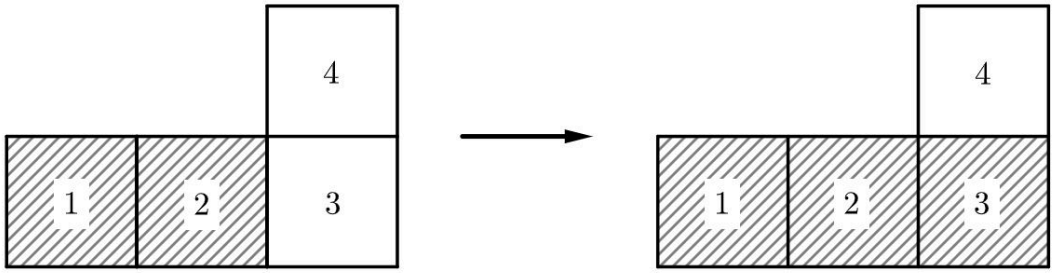

(a) Expansion: Cells 1 and 2 are occupied with gas and then the cluster expands to cell 3. This occurred because the gas pressure over cells 1 and 2 was greater than the drainage threshold, i.e., $P_{1,2} > T_3^e$.

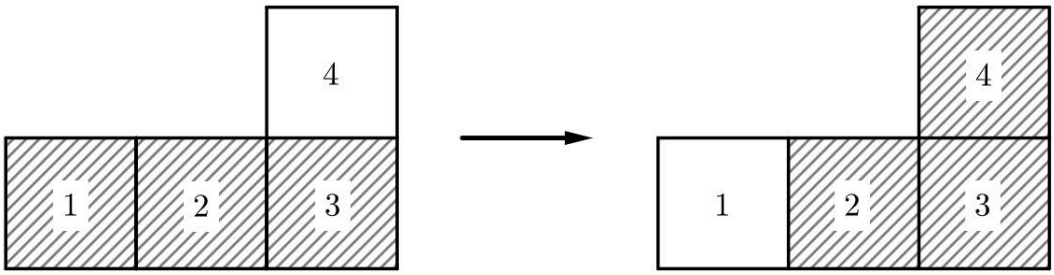

(b) Mobilization: Cells 1, 2 and 3 are occupied with gas and after the cluster mobilized the resulting cluster includes cells 2, 3 and 4. This occurred because the threshold for imbibition in cell 1 was greater than the threshold for drainage in cell 4 and the condition for expansion was met, i.e., $T_1^t > T_4^e$ and $P_{1,2,3} > T_4^e$.

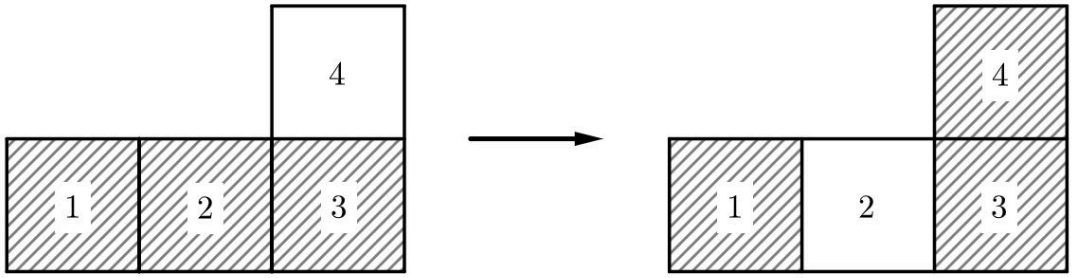

(c) Fragmentation: The gas from cell 2 moved to cell 4, via cell 3. In this event the threshold for imbibition in cell 2 was greater than the threshold for drainage in cell 4 and the condition for expansion was met, i.e., $T_2^t > T_4^e$ and $P_{1,2,3} > T_4^e$

Figure 4.4: A visual of the three processes. The crosshatched cells represent cells where $S_g \geq S_{gcr}$ and the rest are cells where $S_g < S_{gcr}$

or mobilize/fragment. This implementation occurs between the time steps for the heat transfer equation. So Macro-IP has a smaller time step, but we assume everything happens instantaneously [18].

During the process, multiple clusters can join together to form one or break apart into separate clusters (due to fragmentation). After Macro-IP, if any cluster that has reached the extractor, then the vapor is removed from the system. Areas around the heater will eventually dry out and form a dry path connected to an extractor. To enhance NAPL recovery, we assume that dried out regions adjacent to the extractors act as spatial extensions of the extractor [21]. Thus, a cluster just needs a dry path to the extractor for it to be removed.

Chapter 5

Numerical model

In this Chapter, we will outline the numerical scheme used for solving (3.2). The heat transfer equation is solved using an implicit cell centered finite difference scheme as shown in Figure 5.1. We will be using a staggered grid where temperature is located at the cell centers and the thermal conductivity is at the edge centers. In our discretization we will use a uniform spatial grid and time step.

First, we discretize (3.2) using a backward finite difference for the time derivative and a central difference scheme for the spatial derivative. This defines a a linear system of equations to be solved to update the temperatures.

The coefficients $(\rho C_p)_e$ and λ depend on the local gas, water and NAPL saturations. When we discretize (3.2) we will use lagged values for the coefficients, in other words, we use the value of the coefficient at time step l. This ensures that the system of equations is linear, which is easy to solve in MATLAB. If we were to use the value at time step $l+1$, we

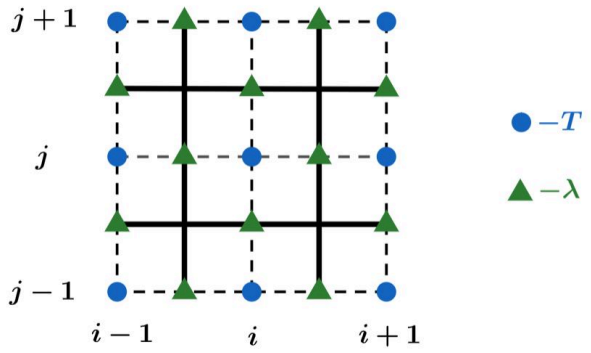

Figure 5.1: The grid choice that we will use for the numerical model where temperature is at the cell center and thermal conductivity is at the edge center.

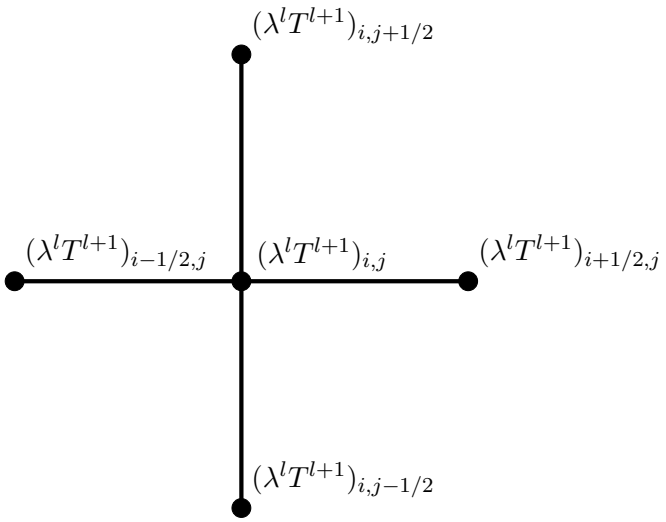

Figure 5.2: A 5 point stencil for the discretization of the outer derivative.

would get a coupled system of cubic equations, which can be difficult to solve on a laptop when there are thousands of nodes [1].

5.1 Discretization

First we will discretize the time and spatial derivatives separately and then construct a linear system for the temperature at time $n+1$.

For the time derivative we will use a first order backward difference. The discretization is

$$(\rho C_p)_e \frac{\partial T}{\partial t}(x_{ij}, t_l) \approx ((\rho C_p)_e)^l_{i,j} \frac{T^{l+1}_{i,j} - T^l_{i,j}}{\Delta t}. \tag{5.1}$$

For the inner and outer derivatives, we will use a central difference. For the outer spatial derivative we get

$$\begin{aligned}\nabla \cdot (\lambda \nabla T) \approx & \frac{1}{\Delta x}\left((\lambda^l \nabla T^{l+1})_{i+1/2,j} - (\lambda^l \nabla T^{l+1})_{i-1/2,j}\right) \\ & + \frac{1}{\Delta z}\left((\lambda^l \nabla T^{l+1})_{i,j+1/2} - (\lambda^l \nabla T^{l+1})_{i,j-1/2}\right).\end{aligned}$$

We use a central difference again for the inner derivative to obtain

$$\begin{aligned}((\rho C_p)_e)^l_{i,j} \frac{T^{l+1}_{i,j} - T^l_{i,j}}{\Delta t} = & \frac{1}{\Delta x}\left(\lambda^l_{i+1/2,j}\frac{T^{l+1}_{i+1,j} - T^{l+1}_{i,j}}{\Delta x} - \lambda^l_{i-1/2,j}\frac{T^{l+1}_{i,j} - T^{l+1}_{i-1,j}}{\Delta x}\right) \\ & + \frac{1}{\Delta z}\left(\lambda^l_{i,j+1/2}\frac{T^{l+1}_{i,j+1} - T^{l+1}_{i,j}}{\Delta z} - \lambda^l_{i,j-1/2}\frac{T^{l+1}_{i,j} - T^{l+1}_{i,j-1}}{\Delta z}\right) - Q^l_{i,j}.\end{aligned}$$

[1] Our goal was to build a computational model which could be run fairly quickly on simple hardware.

Collecting the temperature unknowns together, the discretization of (3.2) becomes

$$\begin{aligned}((\rho C_p)_e)^l_{i,j}\,\frac{T^{l+1}_{i,j}-T^l_{i,j}}{\Delta t} =&\frac{\lambda^l_{i+1/2,j}}{\Delta x^2}T^{l+1}_{i+1,j}+\frac{\lambda^l_{i-1/2,j}}{\Delta x^2}T^{l+1}_{i-1,j}+\frac{\lambda_{i,j+1/2}}{\Delta z^2}T^{l+1}_{i,j+1}+\frac{\lambda^l_{i,j-1/2}}{\Delta z^2}T^{l+1}_{i,j-1}\\ &-\left(\frac{\lambda^l_{i+1/2,j}}{\Delta x^2}+\frac{\lambda^l_{i-1/2,j}}{\Delta x^2}+\frac{\lambda_{i,j+1/2}}{\Delta z^2}+\frac{\lambda^l_{i,j-1/2}}{\Delta z^2}\right)T^{l+1}_{i,j}-Q^l_{i,j}.\end{aligned}$$

Then rearranging gives

$$\begin{aligned}T^l_{i,j}=&\left[\frac{\Delta t}{(\rho C_p)^l_{i,j}}\left(\frac{\lambda^l_{i+1/2,j}}{\Delta x^2}+\frac{\lambda^l_{i-1/2,j}}{\Delta x^2}+\frac{\lambda_{i,j+1/2}}{\Delta z^2}+\frac{\lambda^l_{i,j-1/2}}{\Delta z^2}\right)+1\right]T^{l+1}_{i,j}\\ &-\frac{\Delta t}{(\rho C_p)^l_{i,j}}\left(\frac{\lambda^l_{i+1/2,j}}{\Delta x^2}T^{l+1}_{i+1,j}+\frac{\lambda^l_{i-1/2,j}}{\Delta x^2}T^{l+1}_{i-1,j}+\frac{\lambda_{i,j+1/2}}{\Delta z^2}T^{l+1}_{i,j+1}\right.\\ &\left.+\frac{\lambda^l_{i,j-1/2}}{\Delta z^2}T^{l+1}_{i,j-1}-Q^l_{i,j}\right).\end{aligned}\tag{5.2}$$

This is the linear system of equations for to solve for $T^{l+1}_{i,j}$.

We use ghost cells beyond the boundary to evaluate the centered difference scheme for the points outside the domain. For $i=1$ and $i=N_x+1$ we get

$$T_{0,j}=T_{1,j}-\Delta x f_{L,j} \text{ and } T_{N_x+1,j}=T_{N_x,j}+\Delta x f_{R,j}.$$

For the top and bottom wall, there is no heat flux so we get

$$T_{i,0}=T_{i,1} \text{ and } T_{i,N_z+1}=T_{i,N_z}$$

5.1.1 Thermal conductivity

For the thermal conductivity, we are given the values at the cell-center but we want to use the value at the edge center. We can approximate the value at the edge center by taking the mean of two cell center values. We have a few choices for taking the mean such as arithmetic, geometric or harmonic mean. We follow the standard approach in CFD and use the harmonic mean. For the harmonic mean we get

$$\lambda_{i\pm1/2,j}=\frac{2\lambda_{i,j}\lambda_{i\pm1,j}}{\lambda_{i,j}+\lambda_{i\pm1,j}}\tag{5.3}$$

$$\lambda_{i,j\pm1/2}=\frac{2\lambda_{i,j}\lambda_{i,j\pm1}}{\lambda_{i,j}+\lambda_{i,j\pm1}}\tag{5.4}$$

To compute the mean at the boundary, $i=1,N_x$ or $j=1,N_z$, we again use ghost points as needed.

5.2 Solving for $T_{i,j}^{l+1}$

To solve (5.2) we first define the quantities

$$\begin{aligned}
\Theta =& 1 - (\theta_x^+ + \theta_x^- + \theta_z^+ + \theta_z^-) \\
\theta_x^+ =& -\frac{\Delta t}{((\rho C_p)_e)_{i,j}^l} \frac{\lambda_{i+1/2,j}^l}{\Delta x^2} \\
\theta_x^- =& -\frac{\Delta t}{((\rho C_p)_e)_{i,j}^l} \frac{\lambda_{i-1/2,j}^l}{\Delta x^2} \\
\theta_z^+ =& -\frac{\Delta t}{((\rho C_p)_e)_{i,j}^l} \frac{\lambda_{i,j+1/2}^l}{\Delta z^2} \\
\theta_z^- =& -\frac{\Delta t}{((\rho C_p)_e)_{i,j}^l} \frac{\lambda_{i,j-1/2}^l}{\Delta z^2}
\end{aligned}$$

We want to represent T^l, T^{l+1} and Q^l as vectors to organize the values from left to right and then top to bottom. We will denote the vectors as $\vec{T}^l$, $\vec{T}^{l+1}$ as the temperature at time levels l and $l+1$ and $\vec{Q}^l$ as the source or sink term in each cell at time level l.

For the boundary, we will add it to $\vec{Q}_{i,j}^l$. So we instead solve the following

$$\vec{T}^l = A \cdot \vec{T}^{l+1} + \vec{B}^l \tag{5.5}$$

where A is sparse $N_x \times N_z$ tridiagonal block matrix given by

$$\begin{bmatrix}
D-L & U & & & & \\
L & D & U & & & \\
& \ddots & \ddots & \ddots & & \\
& & L & D & U & \\
& & & L & D-U &
\end{bmatrix} \tag{5.6}$$

The entries of A are the $N_x \times N_z$ matrices given by the following.

$$D = \begin{bmatrix}
\Theta - \theta_x^- & \theta_x^+ & & & & \\
\theta_x^- & \Theta & \theta_x^+ & & & \\
& \ddots & \ddots & \ddots & & \\
& & \theta_x^- & \Theta & \theta_x^+ & \\
& & & \theta_x^- & \Theta - \theta_x^+ &
\end{bmatrix}$$

$$U = \begin{bmatrix} \theta_z^+ & & & & \\ & \theta_z^+ & & & \\ & & \ddots & & \\ & & & \theta_z^+ & \\ & & & & \theta_z^+ \end{bmatrix}, L = \begin{bmatrix} \theta_z^- & & & & \\ & \theta_z^- & & & \\ & & \ddots & & \\ & & & \theta_z^- & \\ & & & & \theta_z^- \end{bmatrix}$$

The vectors for the system are given by

$$\vec{T}^l = \begin{bmatrix} T_{1,1}^l \\ T_{2,1}^l \\ \vdots \\ T_{N_x,1}^l \\ \hdashline T_{1,2}^l \\ T_{2,2}^l \\ \vdots \\ T_{N_x,2}^l \\ \hdashline \vdots \\ \vdots \\ \vdots \\ \vdots \\ \hdashline T_{1,N_z}^l \\ T_{2,N_z}^l \\ \vdots \\ T_{N_x,N_z}^l \end{bmatrix}, \quad \vec{T}^{l+1} = \begin{bmatrix} T_{1,1}^{l+1} \\ T_{2,1}^{l+1} \\ \vdots \\ T_{N_x,1}^{l+1} \\ \hdashline T_{1,2}^{l+1} \\ T_{2,2}^{l+1} \\ \vdots \\ T_{N_x,2}^{l+1} \\ \hdashline \vdots \\ \vdots \\ \vdots \\ \vdots \\ \hdashline T_{1,N_z}^{l+1} \\ T_{2,N_z}^{l+1} \\ \vdots \\ T_{N_x,N_z}^{l+1} \end{bmatrix}, \quad \vec{B}^l = \begin{bmatrix} \bar{Q}_{1,1}^l + \bar{f}_{L,1} \\ \bar{Q}_{2,1}^l \\ \vdots \\ \bar{Q}_{N_x,1}^l + \bar{f}_{R,2} \\ \hdashline \bar{Q}_{1,2}^l + \bar{f}_{L,2} \\ \bar{Q}_{2,2}^l \\ \vdots \\ \bar{Q}_{N_x,2}^l + \bar{f}_{R,2} \\ \hdashline \vdots \\ \vdots \\ \vdots \\ \vdots \\ \hdashline \bar{Q}_{1,N_z}^l + \bar{f}_{L,N_z} \\ \bar{Q}_{2,N_z}^l \\ \vdots \\ \bar{Q}_{N_x,N_z}^l + \bar{f}_{R,N_z} \end{bmatrix}$$

where

$$\bar{Q} = \frac{\Delta t}{(\rho C_p)_e} Q$$

Additionally, we have added the flux terms from the boundary condition to the vector $\vec{B}^l$ and the terms $f_{L,j}$ and $f_{R,j}$ are given by

$$\bar{f}_{L,j} = \Delta x * \left(\frac{\Delta t}{(\rho C_p)_e} \right) \frac{\lambda_{1/2,j}}{\Delta x^2} f_{L,j}$$

$$\bar{f}_{R,j} = \Delta x * \left(-\frac{\Delta t}{(\rho C_p)_e} \right) \frac{\lambda_{1/2,j}}{\Delta x^2} f_{R,j}$$

Lastly, we can solve for $\vec{T}^l$

$$T^{\vec{l+1}} = A^{-1} \left(\vec{T}^l - \vec{B} \right) \tag{5.7}$$

The matrix A has state-dependent parameters, so it needs to be frequently recomputed, but it is always strongly diagonally dominant and hence invertible.

5.2.1 Higher-order extensions

The method as presented is only first-order in time. A simple way to improve this is to store and use the output from previous time steps to determine the new slope to higher order.

A simple implicit method with second-order accuracy is BDF2 [3]:

$$T_{n+2} - \frac{4}{3}T_{n+1} + \frac{1}{3}T_n = \frac{2}{3}\Delta t f(t_{n+2}, T_{n+2}) \tag{5.8}$$

The formulation using this is identical to that of equation 5.7, except that now we replace T^l with $4/3T^l - 1/3T^{l-1}$. To start, we can take one step with the first-order method (possibly with a reduced time step). We use BDF2 in the final version of our code to obtain a second-order method in both time and space.

5.3 Solution process

At the beginning of each time step, we use the heat transfer equation to compute the temperature distribution. Next, we compute the moles of gas produced and compute the new gas saturation. Then, we check if any cells have reached critical gas saturation. If so, Macro-IP is invoked to simulate the movement of gas. Finally, we update the thermal properties and repeat this process.

We have two criteria to choose the time step. Firstly, we must ensure that a stability criterion is satisfied. This can be done in advance of taking a step, and in practice can be done before beginning the computation. However, we must also make sure that we can never generate more gas in a time step than would fill a cell,

$$V_g \leq V_{cell} \tag{5.9}$$

where V_g is the gas volume and V_{cell} is the void volume of the cell. A loose upper bound for this can be found before the computation by ensuring that the time step is not so large that the heat flux from the heater could generate too much gas in the adjacent cell in one step. This calculation simply assumes that all the heat from the heater goes in to boiling a fully water saturated cell at the boiling temperature.

First, using the ideal gas law and criterion in (5.9), the moles of water produced has to satisfy

$$n_{g,w} \leq \frac{V_{cell} P_g}{RT} \tag{5.10}$$

Then, combining this with the energy balance equation we get

$$Q \leq \frac{L_w V_{cell} P_g}{RTV\Delta t} \tag{5.11}$$

Lastly, rearranging we get

$$\Delta t \leq \frac{L_w V_{cell} P_g}{RTVQ} \tag{5.12}$$

In a 0.1m $\times$ 0.05m cell fully saturated with water, this gives a time step restriction of

$$\Delta t \leq 3.9765\text{e+}04\text{s} \tag{5.13}$$

which is about 0.46 days.

Too large a time step can also lead to instabilities related to the Macro-IP stage. If the time step is too large, it can immediately become unreasonably high. In practice, one can reduce the time step whenever irregularities are detected in the temperature and recompute.

Chapter 6

Exact and asymptotic solutions

To better understand the dynamics of this problem, we can construct an exact solution in a special case. This will give us a solution to compare with for our convergence studies and insight into what happens more generally.

We will focus on the simplified geometry of a semi-infinite one-dimensional domain. From the simulation shown in Figure 1.2 presented in the Introduction, this should be reasonable for times until the heat has diffused well into the domain. If there is little NAPL in any cell, it is both vaporized instantly and has very little impact on the material parameters. Thus, we can consider the classical Stefan problem of heating in two domains with a moving front between them, where a phase change occurs.

Impact on depth on co-boiling and boiling temperatures Phase change occurs when we meet the co-boiling condition (3.8). However, seeing that the Antoine equation is temperature dependent and the water pressure only depth dependent, these temperatures are simply functions of z. From Figure 3.2 we see that the temperatures needed for phase change increase by about 2°C per m of depth. We will see in the exact solution that, for reasonable time and space intervals, the solution is quite steep at this point and a change of 2C occurs on a scale of cm.

Thus, it seems reasonable to consider a one-dimensional approximation in the x direction.

Impact of loss of NAPL on material parameters In most settings [22], typical NAPL saturation is on the order of 0.05 or less. In all of our numerical simulations, once the co-boiling temperature is reached, the NAPL is boiled off within 30 minutes. This is essentially instantaneous since we are solving the problem on a time scale of 6-9 months. Values of S_n of this magnitude have very little impact on the specific heat capacity or thermal conductivity at a point. Using Dalton's law and the discussion in Section 3.1.2 on the energy balance, we can calculate precisely how S_g and S_w change in a cell once S_n is reduced to zero. Figure 6.1 shows the relative changes in the parameters before and after the NAPL is completely

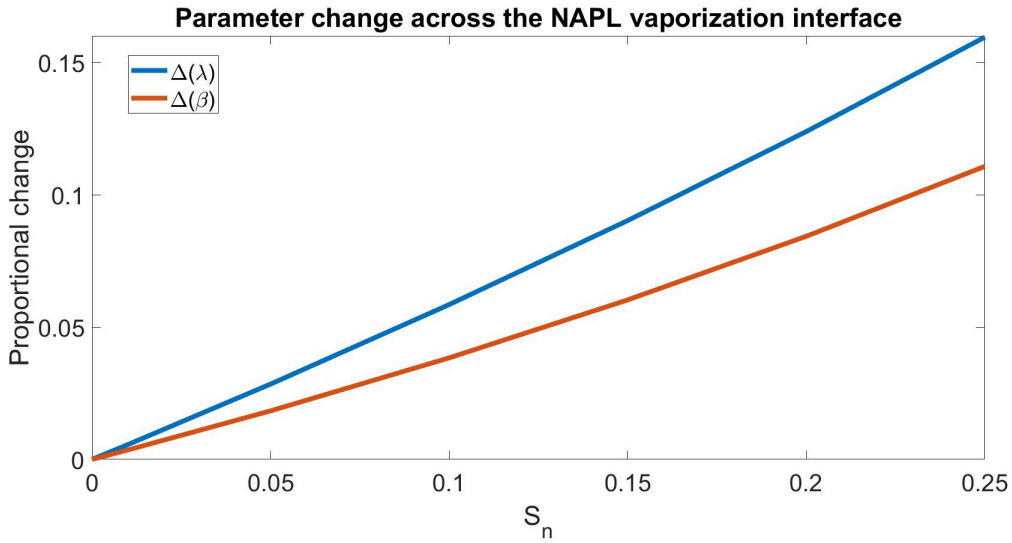

Figure 6.1: Proportional change in the parameters λ and $\beta = \lambda/(\rho C_p)_e$ as a function of the NAPL saturation.

removed from a cell. Recall also that the gaseous NAPL is only removed after the water has boiled or the gas is redistributed via Macro-IP.

Given that NAPL in low concentrations has very little impact on the thermal behaviour of the system, we can ignore its impact in a simplified model. Instead, we will track when the co-boiling has occurred and use that to estimate a bound for then NAPL may be removed.

6.1 Nondimensionalization

First we introduce the following change of variables:

- $t = t_0\tau$
- $x = L_0 y$
- $\theta = \frac{T - T_a}{\Delta T}$.

Here, t_0, L_0 and ΔT are scales to be determined and T_a is initial ground temperature.

Making these substitutions and dropping z derivatives, the heat transfer equation becomes

$$\begin{aligned}(\rho C_p)_e \frac{\Delta T}{t_0}\frac{\partial\theta}{\partial\tau} &= \frac{1}{L_0}\frac{\partial\theta}{\partial y}\left(\frac{\lambda}{L_0}\frac{\partial\theta}{\partial y}(\Delta T\theta + T_a)\right)\\ \frac{\Delta T(\rho C_p)_e}{t_0}\frac{\partial\theta}{\partial\tau} &= \frac{\Delta T\lambda}{L_0^2}\frac{\partial^2\theta}{\partial y^2}\\ \frac{\partial\theta}{\partial\tau} &= \frac{t_0\lambda}{L_0^2(\rho C_p)_e}\frac{\partial^2\theta}{\partial y^2}\end{aligned}$$

Defining $\beta = \frac{\lambda}{(\rho C_p)_e}$ we set $\frac{t_0\beta}{L_0^2} = 1$ to relate the time and space scales. We set $\Delta T = T_B - T_a$ as the difference between the boiling and ambient temperatures.

To determine the length-scale we will use the boundary condition.

$$\begin{aligned} \frac{\Delta T}{L_0}\frac{\partial\theta}{\partial y}\bigg|_{y=0} &= -\frac{Q}{\lambda} \\ \frac{\partial\theta}{\partial y}\bigg|_{y=0} &= -\frac{QL_0}{\Delta T\lambda} \end{aligned}$$

and set

$$\frac{QL_0}{\Delta T\lambda} = 1 \qquad \Rightarrow \qquad L_0 = \frac{\Delta T\lambda}{Q}\,.$$

The time scale is then set by the relation

$$t_0 = \frac{L_0^2}{\beta}\,.$$

Typical values for this problem in saturated soil are $\beta = 9.9378e-07$ and for dry soil $\beta = 4.3275e-07$.

The complete nondimensionalized problem is

$$\begin{cases} \dfrac{\partial\theta}{\partial\tau} = \dfrac{\partial^2\theta}{\partial y^2} \\ \theta(y,0) = 0 \\ \dfrac{\partial\theta}{\partial y}\bigg|_{y=0} = -1 \\ \lim_{y\to\infty}\theta(y,\tau) = 0 \end{cases}$$

This system has no free parameters, so it only needs to be solved once. However, it is only valid for $\theta(0,\tau) \leq 1$. At that point the water boils off and we need to introduce a second domain and a Stefan condition connecting them.

First, we will derive the similarity solution for the constant temperature and constant heat flux boundary conditions.

6.2 Derivation of similarity solution

Similarity solutions are a common feature of many PDE and appear even when they are not exact solutions to the problem [5].

We consider the problem with a Neumann condition at $y = 0$

$$\begin{cases} \dfrac{\partial \theta}{\partial \tau} = \dfrac{\partial^2 \theta}{\partial y^2} \\ \theta(y, 0) = 0 \\ \left.\dfrac{\partial \theta}{\partial y}\right|_{y=0} = -1 \\ \lim_{y\to\infty} \theta(y, \tau) = 0 \end{cases} \tag{6.1}$$

We seek a solution of the form $\theta(y, \tau) = \tau^p f(z)$ where $z = y\tau^q$. Substituting this into the PDE gives

$$\begin{aligned} p\tau^{p-1} f(z) + \tau^p f'(z) * qy\tau^{q-1} =& \tau^p f''(z) * \tau^{zq} \\ \tau^p \left(\frac{p}{\tau} f(z) + \frac{qz}{\tau} f'(z) \right) =& \tau^p (f''(z)\tau^{zq}) \end{aligned}$$

This is only balanced for $q = -1/2$. Then we use the Neumann boundary condition to find p. The boundary condition is for $\theta(y, t)$ constant and the boundary condition for $f(z)$ is also expected to be constant, i.e. $\tau^p f'(0)/\sqrt{\tau}$ is constant. We can conclude $p = 1/2$ as then

$$\frac{\partial \theta}{\partial y} = \sqrt{\tau} \frac{df}{dy} \frac{dz}{dy} = \frac{\sqrt{\tau}}{\sqrt{\tau}} f' = f'(z)\,.$$

Thus the constant boundary condition can be satisfied at $z = 0$ for all τ.

For $\theta(y, \tau) = \sqrt{\tau} f(z)$ the partial derivatives in the PDE are

$$\begin{aligned} \frac{\partial \theta}{\partial \tau} &= -\frac{1}{2\tau} f(z) - \frac{z}{2\tau} f'(z), \\ \frac{\partial^2 \theta}{\partial y^2} &= \frac{1}{\tau} f''(z). \end{aligned}$$

Plugging them into the PDE gives the following ODE

$$2f''(z) + zf'(z) - f(z) = 0.$$

The solution to this is

$$f(z) = c_1 z - c_1 \exp\left(-\frac{z^2}{4}\right) - c_2 \frac{\sqrt{\pi} z}{2} \operatorname{erf}\left(\frac{z}{2}\right)$$

so the general solution to the PDE is

$$\begin{aligned}\theta(y,\tau) =& \sqrt{\tau}\left(c_1\frac{y}{\sqrt{\tau}} - c_1\exp\left(-\frac{y^2}{4\tau}\right) - c_2\frac{\sqrt{\pi}y}{2\sqrt{\tau}}\operatorname{erf}\left(\frac{y}{2\sqrt{\tau}}\right)\right)\\ =& c_1 y - c_1\sqrt{\tau}\exp\left(-\frac{y^2}{4\tau}\right) - c_2\frac{\sqrt{\pi}y}{2}\operatorname{erf}\left(\frac{y}{2\sqrt{\tau}}\right)\end{aligned}$$

The boundary conditions give that $c_1 = -1$ and $c_2 = -\frac{2}{\sqrt{\pi}}$. So we get

$$\theta(y,\tau) = y\left(\operatorname{erf}\left(\frac{y}{2\sqrt{\tau}}\right) - 1\right) + \frac{2\sqrt{\tau}}{\sqrt{\pi}}\exp\left(-\frac{y^2}{4\tau}\right)$$

From this we can find the time that co-boiling is reached as there $T(0,t) = T_{cb}$:

$$\theta(0,\tau_{cb}) = \frac{T_b - T_{cb}}{T_b - T_a} = \theta_{cb} = \frac{2\tau_{cb}}{\sqrt{\pi}} \Rightarrow \tau_{cb} \simeq 0.379\ldots$$

Similarly we can find the time at which boiling first occurs with

$$\theta(0,\tau_b) = 1 \Rightarrow \tau_b = \frac{\pi}{4}$$

Hence this problem is only defined over the range $0 \leq \tau \leq \tau_b \simeq 0.7854\ldots$.

Because the solution is monotonically decreasing, here is only NAPL remaining on $y > y_{cb}$ such that $\theta(y_{cb},\tau) = \theta_{cb}$. This front y_{cb} will satisfy

$$\theta(y_{cb},\tau) = \theta_{cb} = y_{cb}\left(\operatorname{erf}\left(\frac{y_{cb}}{2\sqrt{\tau}}\right) - 1\right) + \frac{2\sqrt{\tau}}{\sqrt{\pi}}\exp\left(-\frac{y_{cb}^2}{4\tau}\right).$$

This can be solved asymptotically as $\tau \to \infty$ to find that $y_{cb} \simeq \sqrt{\tau\ln(\tau)}$ but that is not helpful as this problem is only defined up until $\tau = \tau_b < 1$ at which time boiling begins. Converting this back to the original coordinates recovers

$$T(x,t) = T_a + \frac{Q}{\lambda}\left(2\sqrt{\frac{\beta t}{\pi}}\exp\left(-\frac{x^2}{4\beta t}\right) + x\left(\operatorname{erf}\left(\frac{x}{2\sqrt{\beta t}}\right) - 1\right)\right) \tag{6.2}$$

This gives us an exact solution profile to compare our numerical solutions to and an estimate of when both co-boiling and boiling will begin (see Figure 6.2).

6.2.1 Removing NAPL from dry soil

If the soil is dry to begin with, then there is no water to boil off, and we can solve the problem as above until all NAPL is removed. This is a much slower process than wet soil heating, and therefore this gives a very loose upper bound to the time it would take.

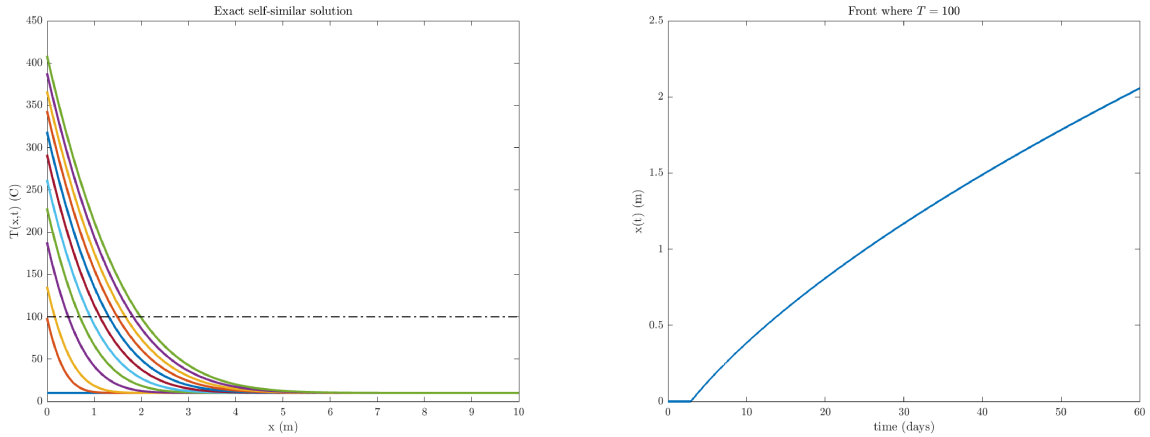

Figure 6.2: Self-similar solution for heating in dry soil (Right). Front where $T = 100$ (Left).

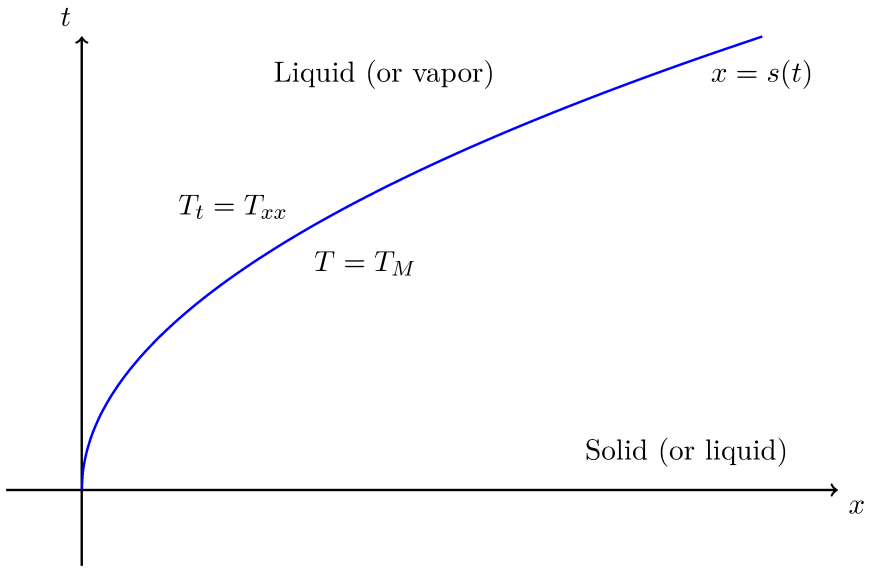

Figure 6.3: The regions in a classical Stefan problem with solid and liquid regions. For our Stefan-like problem we would have liquid in place of solid and vapor in place of liquid.

Using the values of β and λ for dry soil, as mentioned above, we have plotted some temperature profiles and the front location in completely dry soil. Even in dry soil this is an overestimate, as we are never heating an infinite domain. Instead, there are multiple heaters spaced approximately 5-10m apart.

6.3 A Stefan-like problem

A classical Stefan problem describes the melting of a solid [11, 15]. In this case, it is assumed that the solid region is kept at the melting temperature T_M and that one end is raised to a fixed temperature above that T_L (see Figure 6.3). One solves the heat equation with fixed

temperatures at either end of a growing domain. The Stefan condition describes the growth of the melted domain and is derived via conservation of energy, similar to how we describe the phase change in Chapter 3.

This would leave us to solve the system

$$\begin{cases} T(0,t) = T_L \\ T_t = T_{xx} \qquad 0 \leq x \leq s(t) \\ \rho L \frac{ds}{dt} = -\lambda \frac{dT}{dx}(x = s^-, t) \\ T(s^+, t) = T_M \end{cases}$$

with $s(0) = 0$.

There is a self-similar solution due to Neumann, [11] which shows that the interface speed is proportional to $\sqrt{t}$.

A similar problem can be posed in our case *if we ignore the dynamics of the water vapour*. We would solve 6.1 until $t = t_b$ and then solve the *two-phase* Stefan problem

$$\begin{cases} T_x(0,t) = -Q/\lambda \\ T_t = \tilde{\beta} T_{xx} \qquad 0 \leq x \leq s(t) \\ (\rho L)_e \dfrac{ds}{dt} = -\left[\lambda \dfrac{dT}{dx} \right|_{x=s} \\ T(s^+, t) = T_b \\ T_t = T_{xx} \qquad s(t) \leq x \\ \lim_{x \to \infty} T(x,t) = T_a \end{cases}$$

There are no exact solutions to two-phase problems. However, solutions to this problem could give insight into the full problem. Comparison to the Macro-IP approach is an area for future investigation.

Chapter 7

Model verification

Before running simulations, we want to ensure that our model runs accurately. To do this, we will conduct two convergence studies. First, we will check that the 1-dimensional solution defined for a short time converges to the exact solution described in the previous Chapter. Then we will do a full two-dimensional calculation. We will check for convergence before co-boiling begins and afterward. At each point we will check for convergence by decreasing the spatial or time step and observing if the error between the numerical solution and the exact solution decreases with the refinement.

The error will be measured by the L_2-norm. The L_2 norm for a continuous function $f(x)$ in some domain Ω is given by

$$\|f\|_2 = \sqrt{\int_\Omega |f(x)|^2 \, dx} \tag{7.1}$$

For a discrete function represented as a vector, $\vec{f}$, the discrete L_2-norm is

$$\|\vec{f}\|_2 = \sqrt{\frac{1}{N} \sum_{i=1}^{N} |f_i|^2} \tag{7.2}$$

where N is the number of elements in $\vec{f}$. Given the exact and numerical solution of T, denoted as T^e and T^n, the error is given by

$$E = \sqrt{\frac{1}{N_x * N_z} \sum_{i,j} |T^e_{i,j} - T^n_{i,j}|^2} \tag{7.3}$$

where N_x, N_z are the number of points on the grid in x and z.

7.1 Convergence in one spatial dimension

We first compute the convergence to an exact similarity solution of the form REF. We take $S_n = 0, S_w = S_c r$ and $S_g = 1 - S_w$. This is simply heating of dry soil. We first fix $\Delta t = 10$

Δx	Error Ratio
1/5	−−
1/10	2.095930425034272
1/20	2.364850411678903
1/40	2.144649293750456

Δt	Error Ratio
1800	−−
900	2.198127634999944
450	2.282266296739253
225	2.529444966122901

Table 7.1: Errors of T for Δx at 60 days.

Δx	Error
1/5	0.086331546647208
1/10	0.021153979120073
1/20	0.005232204213720
1/40	0.001297693735876
1/80	3.198005106851352e − 04
1/160	7.604655326884321e − 05
1/320	1.519907339805314e − 05

Table 7.2: Errors of T for Δx at 9 days.

and perform a study in Δx then fix Δx and perform a study in Δt. The results are presented in table 7.1.

Next we perform a convergence study when there is co-boiling in the problem. We will implement the model with uniform permeability and initial saturations, and we will only have a constant heat influx at the boundary $x = 0$ (the other three sides will have no heat flux). We will use the following initial values.

$$S_n \equiv 0.01, \quad S_w \equiv 0.99, \quad \phi \equiv 0.3, \quad \text{and} \quad k \equiv 1.03151\text{e} - 12\,.$$

With these parameters, co-boiling begins around 9.5 days, so we will check for convergence at 9 days and 30 days.

Thus we see that for one-dimensional problems the scheme is second-order accurate in both space and time.

Δx	Convergence rate
1/5	–
1/10	2.028958771228965
1/20	2.015438308016146
1/40	2.011468912401539
1/80	2.020705790385569
1/160	2.072217476752661
1/320	2.322899487420808

Table 7.3: Convergence rate for Δx for the two dimensional simulation. This was calculated by $\log(E_2 - E_2)/\log(x_2 - x_1)$ where E_i is the error at step x_i.

Δz	15 days	30 days
1/5	–	–
1/10	0.818936082502286	0.863966639543981
1/20	1.324607589168777	1.321330126252627
1/40	2.380242662981333	2.300397664166125
1/80	0.904679021069586	0.987178648608159
1/160	1.385513148065661	1.700351940937858
1/320	2.320770197646365	2.314879769347753

Table 7.4: Convergence rate for Δz for the two dimensional simulation. This was calculated by $\log(E_2 - E_2)/\log(z_2 - z_1)$ where E_i is the error at time step z_i.

7.2 Convergence in two space dimensions with boiling and Macro-IP

For spatial convergence, we will only check for convergence in the z direction. The numerical solution with grid sizes of $\Delta x = 1/10$ and $\Delta z = 1/640$ was used as the exact solution. We will use a time step of $\Delta t = 720$.

Since our scheme is second-order in space, we would expect the rate of convergence to be second-order. This is the case prior to co-boiling, as shown in Tables 7.1 and 7.3. But after co-boiling we see that the rate of convergence is not exactly second-order. In Table 7.4, we see that we lose an order of accuracy. There are a few factors that contribute to the loss of order. When we discretize the heat transfer equation, we use λ from the previous time step to compute T at the new time step. Also, after co-boiling begins, we start to see jumps in λ which are due to the jump in the saturations. For time, we expect to see second-order convergence since a second order backward difference was implemented. The error ratio in Table 7.1 confirms this.

7.3 Parameter validation

Not all the parameters and implementation details are described in all the related papers. In particular, it is not clear exactly how strong the heaters are or how they are implemented in some cases. However, by inspection of some of the figures we can glean that co-boiling of the NAPL begins around 10 days for the soil and initial parameters used here. From the exact solution, we can estimate the heater power required to do this. For co-boiling to being at 10 days, the power of the heater is $Q_H = 179.395\text{W} \cdot \text{m}^{-2}$. We rounded the power of the heater to $Q_H = 175\text{W} \cdot \text{m}^{-2}$ and with this value, the co-boiling begins at around 10.3 days.

This shows that our results are comparable to those in [21].

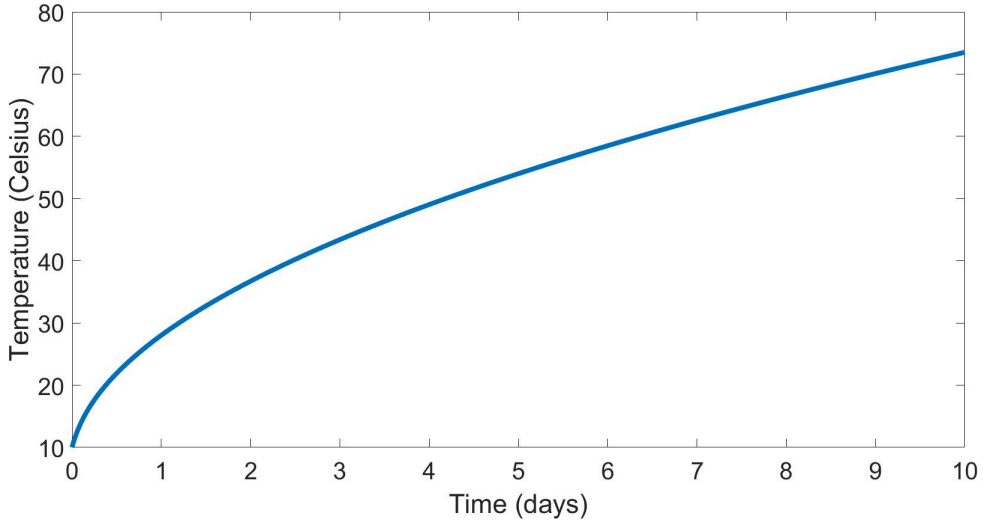

(a) Temperature from 0 to 10 days. This is proportional to $\sqrt{t}$ just as seen in the self-similar solution.

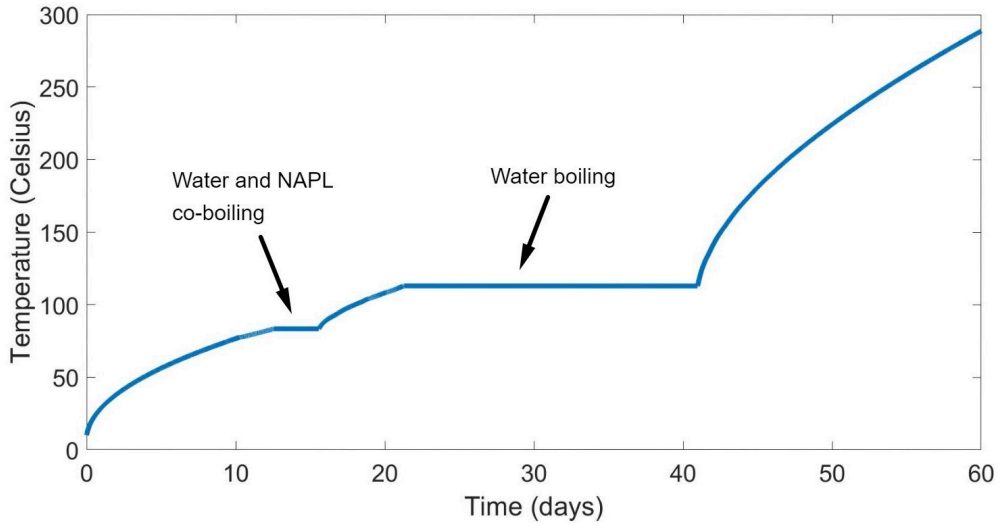

(b) Temperature from 0 to 60 days. First the temperature increases until we reach water and NAPL co-boiling. While water and NAPL are vaporized, the temperature doesn't change in time, as seen by the first plateau which is between 10 and 20 days. All of the NAPL and some water is vaporized in a few days. Then temperature increases until we reach water boiling, this is indicated by the second plateau, which begins just after 20 days. Water is vaporized just after 40 days and afterwards T continues to increase again.

Figure 7.1: Temperature at the boundary cell for a 1D simulation in x.

Chapter 8

Simulations

In this Chapter, we present the results from a few simulations. The objective is to compare simulations with and without Macro-IP implemented, and observe if it has an impact on the completion times. The NAPL recovery with and without MIP for 1D simulations are included. Most of the model parameters were obtained from [21], but some were also acquired from [2] and [20].

8.1 Assumptions

We will run simulations under the following assumptions [21]

1. No gas is present prior to heating (i.e. $S_g \equiv 0$ at $t = 0$)
2. Porosity, thermal conductivity of saturated and thermal conductivity of dry soil are uniform throughout the domain
3. Influence of NAPL on thermal conductivity is neglected
4. Liquid phase NAPL is immobile during heating
5. Water pressures are hydrostatic (i.e. the gradient in the vertical direction is constant)
6. Liquid water is immobile during MIP
7. $S_w \in [S_r, 1]$, i.e. no cells have $S_n > 1 - S_r$. Or we could make the assumption that $S_r = 0$
8. Water can't be vaporized once it reaches S_r
9. Effects of hysteresis are neglected

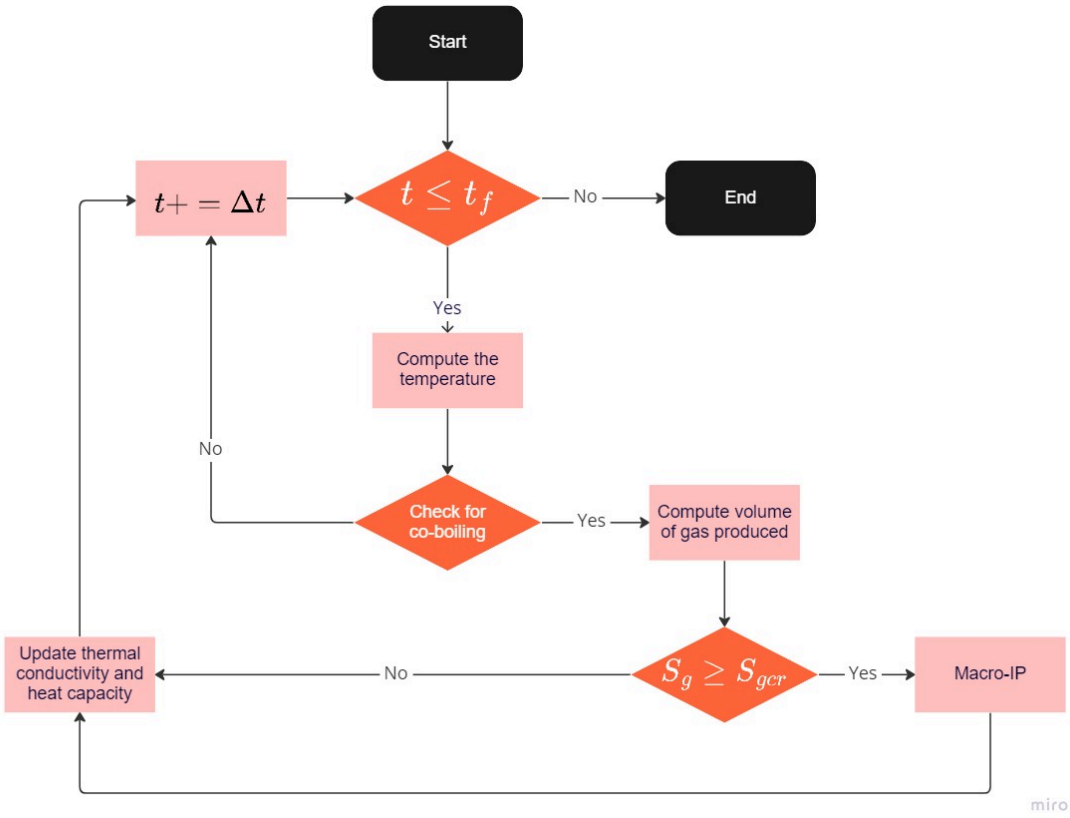

Figure 8.1: A flow chart showing the process of the model.

8.2 Macro-IP vs no Macro-IP

We want to compare simulations with and without Macro-IP implemented. The reason is because we want to determine whether or not implementing it will have a considerable impact on the removal of NAPL. Recall that the dried regions around the heaters act as spatial extensions of the extractors. The simulations without Macro-IP will rely solely on the extension of extractors for NAPL recovery. Simulations ran to 90 days and stopped early if all of the NAPL was removed.

Figures 8.3 and 8.4 shows the NAPL recovery percentage with and without Macro-IP implemented for the one dimensional case. All of the NAPL was removed before 90 days, so we will compare completion times. For the simulations in Figure 8.3, the difference in completion time was less than 3 days, and for the simulations in Figure 8.4, the difference was just over half a day. The time difference is relatively small compared to how long the simulations were running for.

Figures 8.5 and 8.6 shows the NAPL recovery rate with and without Macro-IP for the two dimensional case. There was only one instance where the simulation stopped early due to all of the NAPL being removed, so for the two dimensional simulations we compare the

recovery percentage at 90 days. Similar to the one-dimensional case, there isn't a substantial difference whether or not Macro-IP is implemented.

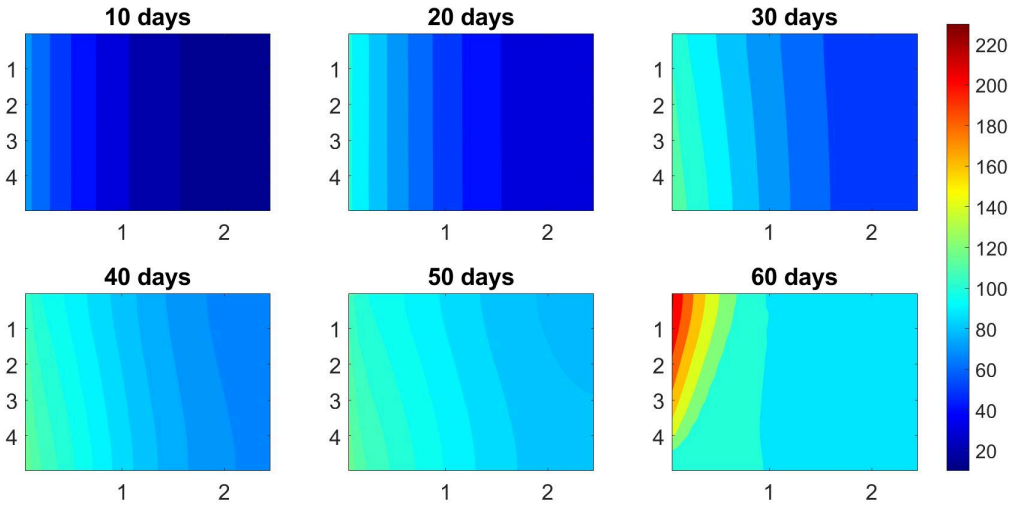

(a) Temperature profiles during the duration of the simulation. The initial temperature is uniformly 10°C. At $t = 60$ days the maximum temperature is just above 223°C. At 10 and 20 days, the temperature appears uniform in z, but by 30 days we see that it is non uniform. This is due to phase change of water occurring along the boundary. During phase change, the temperature doesn't change in time. By 60 days, from $z = 0$ to about 3.5 the water along the boundary has vaporized so the temperature increases again. But from $z = 3.5$ to the bottom there is still water in the cells, so the temperature doesn't change in time yet.

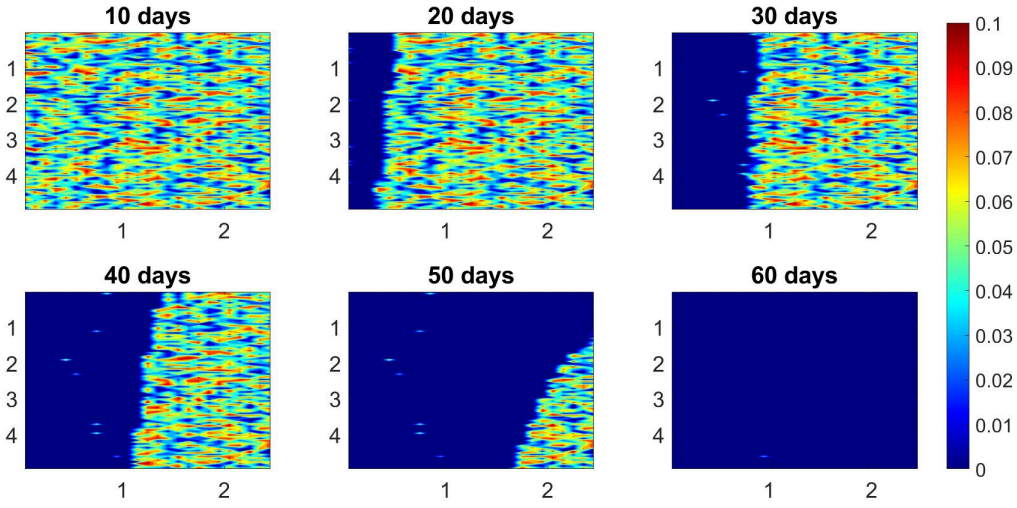

(b) NAPL saturation profiles during the duration of the simulation. The initial saturation was non uniform with an average of 0.0505. The saturation ranged from 0 to 0.1. The vaporization has a nonuniform front, the NAPL towards the top of the domain vaporizes earlier than at the bottom. This is due to the top of the domain having a lower co-boiling temperature than the bottom, as shown in Figure 3.2.

Figure 8.2: Temperature and NAPL profiles for a simulation over a 2.5m × 5m domain.

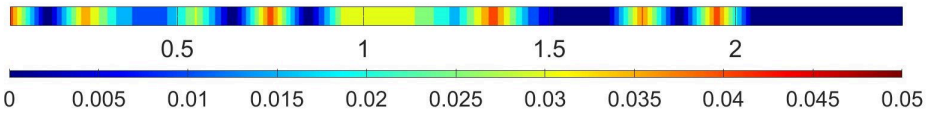

(a) Intial NAPL saturation used in the simulations for Figure 8.3b. The saturation ranged between 0 and 0.05 and the mean is 0.0175.

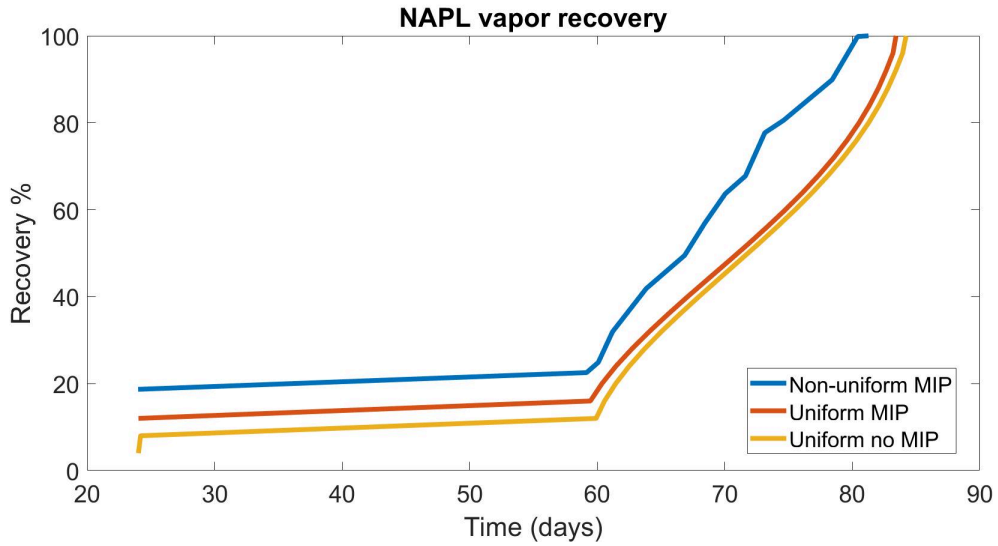

(b) NAPL vapor recovery percentage for three simulations. The blue curve is for the simulation using a nonuniform S_n, as shown in Figure 8.3a, with Macro-IP implemented. For the red and yellow curve, a uniform S_n was used and this value was the mean of the nonuniform S_n. For the red curve, Macro-IP was implemented and for the yellow curve, Macro-IP was not implemented.

Figure 8.3: A comparison of the completion time and recovery percentage for one dimensional simulations in x with and without Macro-IP implemented. For all three simulations, all of the NAPL was recovered, but the completion times varied. The completion times for the blue, red and yellow curves were 81.2750, 83.4333 and 84.2167 days, respectively.

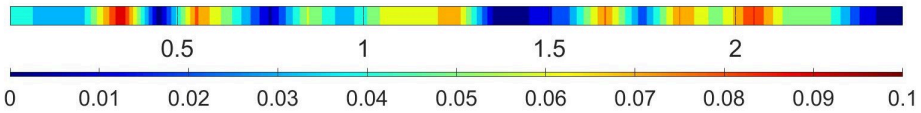

(a) Intial NAPL saturation used in the simulations for Figure 8.4b. The saturation ranged between 0 and 0.1 and the mean is 0.0462.

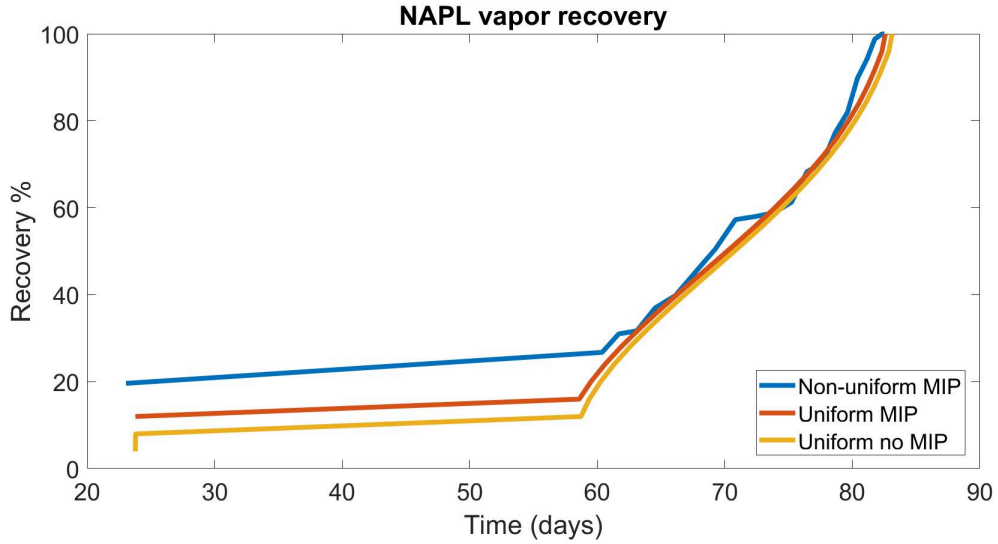

(b) NAPL vapor recovery percentage for three simulations. The blue curve is for the simulation using a nonuniform S_n, as shown in Figure 8.4a, with Macro-IP implemented. For the red and yellow curve, a uniform S_n was used and this value was the mean of the nonuniform S_n. For the red curve, Macro-IP was implemented and for the yellow curve, Macro-IP was not implemented.

Figure 8.4: A comparison of the completion time and recovery percentage for a one dimensional simulations in x with and without Macro-IP implemented. For all three simulations, all of the NAPL was recovered, but the completion times varied. The completion times for the blue, red and yellow curves were 82.5333, 82.5917 and 83.1250 days, respectively.

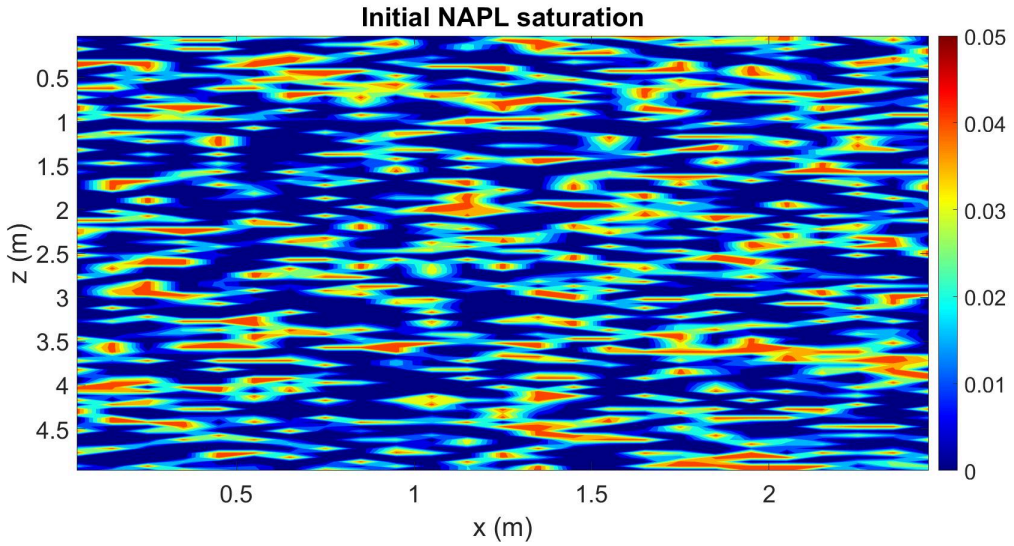

(a) Initial NAPL sauration used in the simulations in Figure 8.5b. The saturation ranged from 0 to 0.05 and the mean is 0.0143.

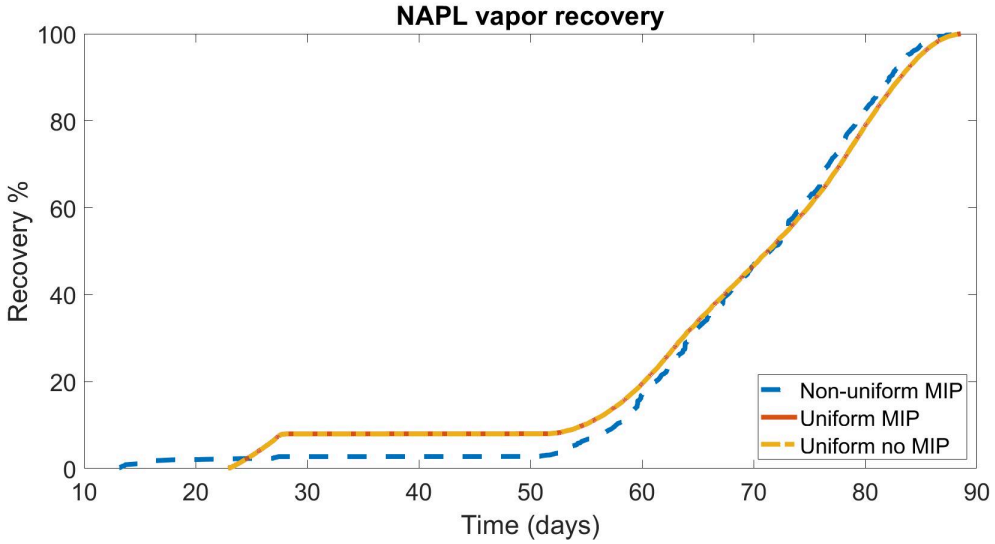

(b) NAPL vapor recovery percentage for three simulations. The blue solid curve is for the simulation using a nonuniform S_n, as shown in Figure 8.5a, with Macro-IP implemented, For the red and yellow dashed curve, S_n was uniformly the mean of the nonuniform S_n. For the red curve, Macro-IP was implemented, and for the yellow curve, it was not implemented.

Figure 8.5: A comparison of the recovery percentage for a two dimensional simulation with and without Macro-IP implemented. The simulations ran up to 90 days and for all three simulations all of the NAPL wasn't removed. The recovery percentage at 90 days for the blue, red and yellow curves were 99.9143, 99.9118 and 99.9553 respectively.

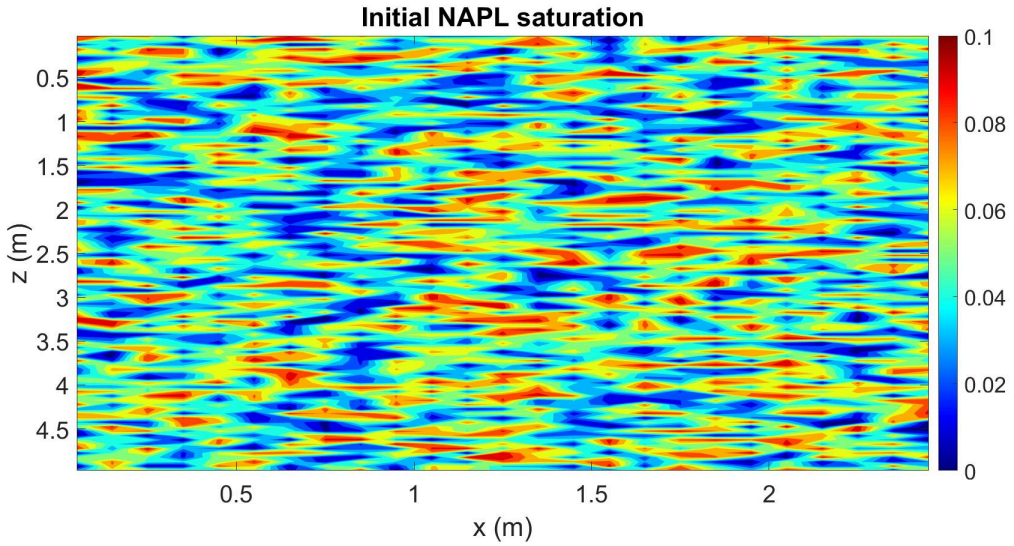

(a) Initial NAPL sauration used in the simulations in Figure 8.6b. The saturation ranged from 0 to 0.1 and the mean is 0.0501.

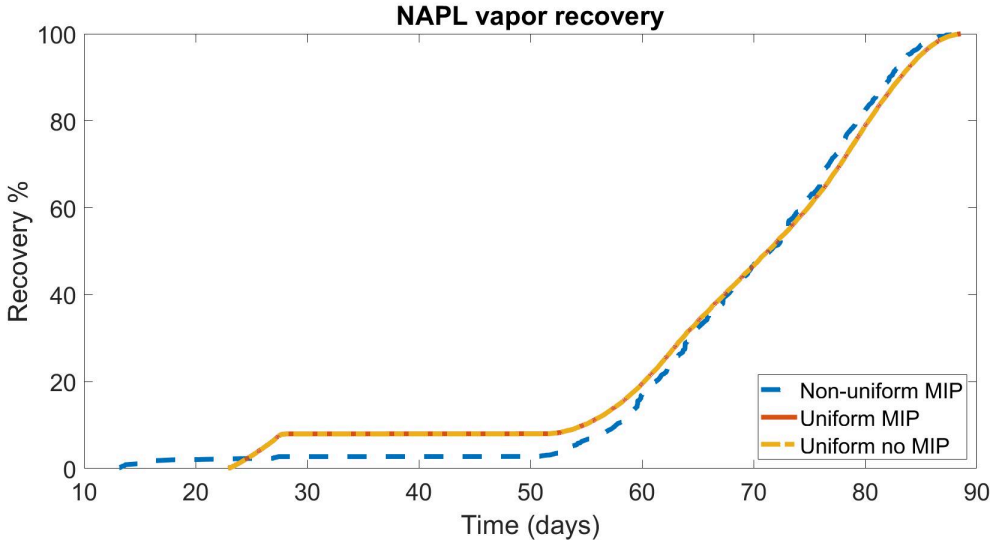

(b) NAPL vapor recovery percentage for three simulations. The blue dashed curve is for the simulation using a nonuniform S_n, as shown in Figure 8.6a, with Macro-IP implemented, For the red solid and yellow dashed curve, S_n was uniformly the mean of the nonuniform S_n. For the red curve, Macro-IP was implemented, and for the yellow curve, it was not implemented.

Figure 8.6: A comparison of the recovery percentage for a two dimensional simulation with and without Macro-IP implemented. The simulations ran up to 90 days and only for one of the three simulations all of the NAPL vapor was removed. The recovery percentage at 90 days for the blue, red and yellow curves were 99.8176, 100 and 99.9554 respectively.

Chapter 9

Conclusion

In this thesis we have presented an implementation of the Macro-IP algorithm and compared the results to simpler models in one dimension. We found that the dynamics of the NAPL front is primarily determined by the time the location reaches a depth-dependent temperature and only weakly on the amount of NAPL initially present. By examining the material parameters, we see that wet soil is much more efficient in removing NAPL. With constant or mildly varying NAPL saturation it makes very little difference whether we actually use the Macro-IP algorithm; the problem is well described by only considering the thermal dynamics and completely ignoring the moisture and gas dynamics. With highly inhomogeneous model parameters, Macro-IP is beneficial and helps to remove the NAPL vapour more quickly.

In general, we can estimate an upper bound on the completion time with Macro-IP implemented. The process of NAPL removal is slightly slower in soils with uniform distributions without Macro-IP implemented. But this difference is relatively small, thus the simulations without Macro-IP can be conducted in lieu of simulations with Macro-IP.

The benefit of running simulations without Macro-IP is that it takes less time than those with Macro-IP. Although compared to continuum methods for gas movement Macro-IP lowers the computational cost, the simulations take a few hours to complete whereas simulations conducted without Macro-IP take less than an hour.

Bibliography

[1] Jørg E. Aarnes, Tore Gimse, and Knut-Andreas Lie. *An Introduction to the Numerics of Flow in Porous Media using Matlab*, pages 265–306. Springer Berlin Heidelberg, Berlin, Heidelberg, 2007.

[2] Richards Alexandra, Jason I. Gerhard, and Bernard H. Kueper. Hydraulic displacement of dense nonaqueous phase liquids for source zone stabilization. *Groundwater*, 50(5):765–774, 2012.

[3] U.M. Ascher and L.R. Petzold. *Computer Methods for Ordinary Differential Equations and Differential-Algebraic Equations*. Other Titles in Applied Mathematics. Society for Industrial and Applied Mathematics (SIAM, 3600 Market Street, Floor 6, Philadelphia, PA 19104), 1998.

[4] Amr Mohamed Badawy and Tarek Al Arbi Omar Ganat. *Capillary Pressure*, pages 79–115. Springer International Publishing, Cham, 2022.

[5] G.I. Barenblatt and B.G. Isaakovich. *Scaling, Self-similarity, and Intermediate Asymptotics: Dimensional Analysis and Intermediate Asymptotics*. Cambridge Texts in Applied Mathematics. Cambridge University Press, 1996.

[6] Brian Berkowitz and Robert P. Ewing. Percolation theory and network modeling applications in soil physics. *Surveys in Geophysics*, 19:23–72, 1998.

[7] R.H. Brooks and A.T. Corey. *Hydraulic properties of porous media*, volume 3 of *Colorado State University Hydrology Paper*. Colorado State University, Fort Collins, Colorado, 1964.

[8] R.H. Brooks and A.T. Corey. Hydraulic properties of porous media and their relation to drainage design. *Transactions of the ASABE*, 7:26–28, 1964.

[9] Stéfan Colombano, Hossein Davarzani, Eric D. van Hullebusch, Ioannis Ignatiadis, Huguen Huguenot, Clément Zornig, and Dominique Guyonnet. *In Situ Thermal Treatments and Enhancements: Theory and Case Study*, pages 149–209. Springer International Publishing, Cham, 2020.

[10] Jean Côté and Jean-Marie Konrad. A generalized thermal conductivity model for soils and construction materials. *Canadian Geotechnical Journal*, 42:443–458, 2005.

[11] John Crank. *Free and Moving Boundary Problems.* OUP, Clarendon, 1984.

[12] Abhijit Y. Dandekar. *Petroleum Reservoir Rock and Fluid Properties.* CRC Press, 2013.

[13] D.W. Depaoli, Herbes S.E., J.H. Wilson, D.K. Solomon, and H.L. Jennings. In situ soil venting - full scale test hill afb, guidance document, 1991.

[14] J. I. Gerhard and B. H. Kueper. Capillary pressure characteristics necessary for simulating dnapl infiltration, redistribution, and immobilization in saturated porous media. *Water Resources Research*, 39(8), 2003.

[15] S.C. Gupta. *The Classical Stefan Problem: Basic Concepts, Modelling and Analysis.* Elsevier Science, 2003.

[16] Xavier Nicolas J. Bénard, Robert Eymard and C. Chavant. Boiling in porous media: Model and simulations. *Transport in Porous Media*, 60(1):1–31, 2005.

[17] Magdalena M.Krol, Kevin G.Mumford, Richard L.Johnson, and Brent E.Sleep. Modeling discrete gas bubble formation and mobilization during subsurface heating of contaminated zones. *Advances in Water Resources*, 34(4):537–549, 2011.

[18] Ian L. Molnar, Kevin G. Mumford, and Magdalena M. Krol. Electro-thermal subsurface gas generation and transport: Model validation and implications. *Water Resources Research*, 55(6):4630–4647, 2019.

[19] Kevin G. Mumford, Paul R. Hegele, and Graham P. Vandenberg. Comparison of two-dimensional and three-dimensional macroscopic invasion percolation simulations with laboratory experiments in gas bubble flow in homogeneous sands. *Vadose Zone Journal*, 14:1–13, 2015.

[20] Kevin G. Mumford, James E. Smith, and Sarah E. Dickson. The effect of spontaneous gas expansion and mobilization on the aqueous-phase concentrations above a dense non-aqueous phase liquid pool. *Advances in Water Resources*, 33(4):504–513, 2010.

[21] Qianli Xie, Kevin G. Mumford, and Bernard H. Kueper. Modelling gas-phase recovery of volatile organic compounds during in situ thermal treatment. *Journal of Contaminant Hydrology*, 234:103698, 2020.

[22] Qianli Xie, Kevin G. Mumford, Bernard H. Kueper, and Chen Zhao. A numerical model for estimating the removal of volatile organic compounds in laboratory-scale treatability tests for thermal treatment of napl-impacted soils. *Journal of Contaminant Hydrology*, 226:103526, 2019.

[23] Shenglai Yang. *Capillary Pressure and Capillary Pressure Curve*, pages 365–412. Springer Berlin Heidelberg, Berlin, Heidelberg, 2017.

[24] Carl L Yaws, Prasad K. Narasimhan, and Chaitanya Gabbula. *Yaws' Handbook of Antoine Coefficients for Vapor Pressure (2nd Electronic Edition)*. Knovel, 2009.